Title: Controls on the hydrogen isotope composition of tetraether lipids in a marine thaumarchaeon

Authors:
W. D. Leavitt[*,†,1,2], S. H. Kopf[3,†,*], Y. Weber[4,§], B. Chiu[1, ‡], J. M. McFarlin[3,4], F. J. Elling [5,6], S. Hoeft-McCann[5,¥], A. Pearson[5,*]

[†]*Contributed equally*; ***Correspondence;***

Affiliations:
1. Dartmouth Earth Sciences; 2. Dartmouth Chemistry; 3. Department of Geological Sciences, University of Colorado Boulder, Boulder, Colorado 80309; 4. Department of Geology & Geophysics, University of Wyoming; 5. Department of Earth & Planetary Sciences, Harvard University; 6. Leibniz-Laboratory for Radiometric Dating and Isotope Research, Kiel University

Current Address:
[§]*Beam Theraputics;* [‡]*c16 biosciences;* [¥]Wellesley College.

Keywords: Archaeal lipids, GDGTs, biphytanes, biomarkers

Abstract

The stable hydrogen isotope composition of persistent biomolecules is used as a paleoenvironmental proxy. While much previous work has focused on plant leaf wax-derived *n*-alkanes, the potential of bacterial and archaeal lipid biomarkers as carriers of H isotope signatures remains underexplored. Here we investigated H isotope distributions in the membrane lipids of the ammonia-oxidizing chemoautotroph *Nitrosopumilus maritimus* strain SCM1. Hydrogen isotope ratios were measured on the biphytane chains of tetraether membrane lipids extracted from steady-state continuous cultures cultivated at slow, medium, and fast growth rates. In contrast to recent work on bacterial fatty acids, where the direction and magnitude of isotopic fractionation varies widely (*ca.* 600 ‰ range) in response to the choice of substrate and pathways of energy metabolism, archaeal biphytane data in the present work are relatively invariant. The weighted average $^{2}H/^{1}H$ fractionation values relative to growth water ($^{2}\varepsilon_{L/W}$) only ranged from -272 to -260 ‰, despite a three-fold difference in doubling times (30.8 hr to 92.5 hr), yielding an average growth-rate effect of 0.2 ‰ hr^{-1}. These $^{2}\varepsilon_{L/W}$ values are more depleted than all heterotrophic archaeal and bacterial lipid H isotope measurements in the literature, and on par with those from other autotrophic archaea, as well as isoproenoid-based lipids in photoautotrophic algae. *N. maritimus* values of $^{2}\varepsilon_{L/W}$ also varied systematically with the number of internal rings (cyclopentyl + cyclohexyl), increasing for each additional ring by 6.4 ± 2.7 ‰. Using an isotope flux-balance model in tandem with a comprehensive analysis of the sources of H in archaeal lipid biosynthesis, we use this observation to estimate the kinetic isotope effects (KIEs) of H incorporation from water; from reducing cofactors such as ferredoxin, and for the transhydrogenation reaction(s) that convert the electron-donor derived NADH into NADPH for anabolic reactions. Consistent with prior studies on bacteria, our results indicate the KIEs of reducing cofactors and transhydrogenation processes in archaea are highly fractionating, while those involving exchange of water protons are less so. When combined with the observation of minimal growth-rate sensitivity, our results suggest biphytanes of autotrophic 3HP/4HB Thaumarchaeota may be offset from source waters by a nearly constant $^{2}\varepsilon_{L/W}$ value. Together with the ring effect, this implies that all biphytanes originating from a common source should have a predictable ordering of their isotope ratios with respect to biphytane ring number, allowing precise reconstruction of the original $\delta^{2}H$ value of the growth water. Collectively, these patterns indicate archaeal biphytanes have potential as paleo-hydrological proxies, either as a complement or an alternative to leaf wax *n*-alkanes.

1. Introduction

The relative abundances of protium (^{1}H) and deuterium (^{2}H) in water track a wide variety of physical, hydrological, and climate parameters (Gat, 1996; Hayes, 2001; Robert, 2001). Certain biomolecules incorporate these isotopes at predictable ratios (δ^2H values) relative to their source water, preserving a record of conditions at the time of synthesis. Indeed some lipid hydrogen isotope compositions can survive in the sedimentary record for millions of years, encoding past changes in Earth system processes, from tectonics to hydroclimate to local ecology (Sessions et al., 2004; Schimmelmann et al., 2006; Sessions, 2016). The H isotopic ratios of biomolecules utilized for reconstructing past environments and ecologies have been studied broadly in photoautotrophic organisms, as well as in a variety of chemoautotrophic and heterotrophic bacteria (e.g., (Sessions et al., 1999; Zhang et al., 2009; Dawson et al., 2015; Sachs and Kawka, 2015; Maloney et al., 2016; Osburn et al., 2016; Sachs et al., 2016, 2017; Wolfshorndl et al., 2019)). To date, however, there are few reports for the archaea (Kaneko et al., 2011; Dirghangi and Pagani, 2013; Wu et al., 2020; Lengger et al., 2021). In part this taxonomic bias originates from the long history of experimental and field study on leaf plant waxes and marine phytoplankton (Estep and Hoering, 1980; Sessions et al., 1999; Sachse et al., 2012; Sachs, 2014), but it also arises from a lack of systematic understanding of how archaeal biomarkers are biosynthesized (Jain et al., 2014; Pearson, 2019; Zeng et al., 2019), how archaeal lipid δ^2H values reflect growth waters, as well as analytical challenges in the H isotope analysis of archaeal ether lipids (Lengger *et al.*, 2021). Unlocking the historical archive of archaeal lipid H isotopes requires examining the biochemical controls on their lipid-water isotope effects ($^2\varepsilon_{L/W}$).

The expression of $^2\varepsilon_{L/W}$ in geostable lipids reflects not only incorporation of environmental water, but also the kinetic isotope effects (KIEs) of enzymes involved in energy conservation, central metabolism, and the pathway(s) of lipid biosynthesis. In plants and eukaryotic algae the $^2\varepsilon_{L/W}$ between growth water and long-chain *n*-alkanes (plant waxes) captures changes in hydroclimate, as many of the biosynthetic and metabolic KIEs are similar between these taxa (Smith and Freeman, 2006; Hou et al., 2008; Sachse et al., 2010, 2012; Kahmen et al., 2011; McInerney et al., 2011), although a quarter of the observed variance could also be due to genetic factors (Bender et al., 2016). Experimental calibration of lipid $^2\varepsilon_{L/W}$ from eukaryotic microalgae therefore focuses on constraining the response to physical parameters such as temperature, salinity, and irradiance (Sachs, 2014; Sachs and Kawka, 2015; van der Meer et al., 2015; Maloney et al., 2016; Sachs et al., 2016, 2017; Wolfshorndl et al., 2019). In contrast to eukaryotic examples, bacterial lipids show considerably more complexity. Multiple taxa have been studied with respect to their $^2\varepsilon_{L/W}$ offsets from growth water, as well as for differences between metabolism-specific processes and use of different substrates (Sessions et al., 1999, 2002; Valentine et al., 2004; Campbell et al., 2009; Zhang et al., 2009; Dawson et al., 2015; Heinzelmann et al., 2015b; Osburn et al., 2016; Leavitt et al., 2016; Campbell et al., 2017; Leavitt et al., 2017; Heinzelmann et al., 2018; Wijker et al., 2019). Such work shows that $^2\varepsilon_{L/W}$ can be exceptionally large in bacteria, varying by several *percent* in

both the positive and negative directions. Broad patterns of $^{2}\varepsilon_{L/W}$ values distinguish bacterial chemoautotrophs (-400‰ to -200‰), oxygen producing photoautotrophs (-250‰ to -150‰), and aerobic and anaerobic heterotrophs (-150‰ to +300‰) (Sessions et al., 2002; Valentine et al., 2004; Kreuzer-Martin et al., 2006; Campbell et al., 2009, 2017; Zhang et al., 2009; Dawson et al., 2015; Heinzelmann et al., 2015; Osburn et al., 2016; Leavitt et al., 2016; Leavitt et al., 2016; Leavitt et al., 2017; Wijker et al., 2019).

Archaea generate some of the most diagenetically robust and structurally diagnostic lipids, yet have been little studied, with currently only a few reports of axenic culture natural abundance lipid $\delta^{2}H$ and enriched isotope studies. The natural abundance lipid $\delta^{2}H$ studies were conducted with a mesophilic halophile (Dirghangi and Pagani, 2013), a thermoacidophile and a single marine sediment sample (Kaneko et al., 2011), and a thermoacidophile and two natural samples (Lengger et al., 2021). The axenic deuterium isotope enrichment study used a methanogen (Wu et al., 2020), as well as a suite of mixed culture studies focused on anaerobic methane oxidizers (Kellermann et al., 2016; Wegener et al., 2016). The archaeal biomarkers most critical to paleoenvironmental reconstructions are the glycerol dibiphytanyl glycerol tetraethers (iGDGTs), compounds that are found as a series of structural homologs containing from zero to eight cyclopentane rings (most commonly ≤ 6; iGDGT-0, -1, … -6); or in the case of crenarchaeol, a lipid believed to be unique to Thaumarchaeota, one cyclohexane and four cyclopentane rings (Oger and Cario, 2013; Pearson and Ingalls, 2013; Schouten et al., 2013; Elling et al., 2017). The primary application of iGDGT biomarkers to date has been marine paleothermometry (Schouten et al., 2002), which requires calibration of iGDGT ring distributions to growth temperature and other environmental forcing, both in the laboratory and in modern core-top samples (e.g., (Kim et al., 2008, 2010; Tierney and Tingley, 2014, 2015; Hurley et al., 2016; Elling et al., 2017; Cobban et al., 2020; Dunkley Jones et al., 2020; Zhou et al., 2020). The ring distributions of thermoacidophiles provide important context to this work by investigating the interaction between temperature changes and other growth determinants such as pH, energy availability, and redox status (Boyd et al., 2011, 2013; Feyhl-Buska et al., 2016; Quehenberger et al., 2020; Zhou et al., 2020; Tourte et al., 2022). Similarly detailed work is needed to understand the $^{2}\varepsilon_{L/W}$ isotope signatures of GDGTs so we may evaluate their potential as hydrologic cycle proxies.

In this study we determined the H isotope fractionation between iGDGTs and growth water for the ammonia-oxidizing archaeal (AOA) chemoautotroph *Nitrosopumilus maritimus* SCM1 (Thaumarchaeota), Strain SCM1 was cultivated continuously under chemically static (chemostat) conditions at a range of cellular doubling times. The growth and metabolic rates were controlled by increasing or decreasing the energy flux (terminal electron acceptor donor delivery rate) of the supply medium; for prior examples of this approach with archaea, see (Hurley et al., 2016; Quehenberger et al., 2020; Zhou et al., 2020). For all trials, we quantified the magnitude of $^{2}\varepsilon_{L/W}$ for the full set of biphytane (BP) hydrocarbons liberated by ether cleavage from acid extractable total iGDGTs. We present values from BP-0, BP-1, BP-2, and BP-3. The results indicate that $^{2}\varepsilon_{L/W}$

for *N. maritimus* remains nearly constant between fast, medium, and slow growth rates. The results suggest that the ubiquitous iGDGTs of mesophilic autotrophs have potential as paleo-hydrological proxies. The hydrogen isotope ratios of mesophilic archaeal iGDGTs and their derivative BPs may be reliably and consistently offset from local growth waters.

2. Methods

2.1 Culture conditions

Continuous (chemostat) cultures of *N. maritimus* SCM1 were grown on modified Synthetic Crenarchaeota Medium with 1 mM NH_4Cl as previously described (Martens-Habbena et al., 2009; Hurley et al., 2016), but with the following modifications: 300 µM α-ketoglutaric acid was added as a H_2O_2 scavenger (Kim et al., 2016; Bayer et al., 2019), and a balance-controller loop was used to maintain a constant dilution rate (my-Control™, Applikon, Delft, the Netherlands). In the 1.6 L reactor temperature was held constant at 28 ºC, and the pH of the initial medium was adjusted to 7.8, which yielded in-situ pH of 7.52 to 7.56 over the course of the experiments at steady state. Nitrite concentrations and pH values for *N. maritimus* remained stable within analytical precision (nitrite ±0.03 mM; pH ±0.01). The *N. maritimus* experiments were run in a single bioreactor and maintained steady state conditions throughout the sampling intervals. The dilution rate was set to yield cell doubling times (T_D) of 30.8, 46.2, and 92.5 h. Upon reaching steady state, the outflow of each bioreactor was collected continuously into a chilled vessel (0 to 4 °C) for between 1 and 4 days. *N. maritimus* cells were isolated by filtration onto combusted 0.3 µm GF-75 glass fiber filters (Sterlitech, Kent, WA, USA). Filters were stored at -80 or -20 °C until processing for lipid analysis.

2.2 Lipid extraction and biphytane preparation

Core iGDGTs were extracted from freeze-dried pellets and filters by acid hydrolysis followed by ultrasonic solvent extraction as described previously (Zhou et al., 2020). Briefly, samples were incubated in 3 N methanolic HCl (33% water content) for 90 min at 65°C. Methyl tert-butyl ether (MTBE) was added at a ratio of 3:2 (acid:MTBE, v:v), and samples were sonicated for 5 min (Qsonica Q500, Newtown, CT, USA). After sonication, *n*-hexane was added at a ratio of 1:1 (MTBE:hexane, v:v), vortexed, and centrifuged (3 min, 15,000 *g*). The organic upper layer was collected, dried under N_2, and separated into two fractions over activated Al_2O_3 by elution with dichloromethane (DCM; non-polar lipids), and DCM:methanol (1:1, v:v; iGDGTs). Ether bonds were cleaved in 57 % HI (4h at 120°), and the resulting alkyl iodides were reduced to alkanes (BPs) with H_2 in the presence of $Pt^{(IV)}O_2$ (Kaneko et al., 2011). Before analysis, BPs were purified over activated Al_2O_3 by elution with *n*-hexane. Samples of *N. maritimus* were collected in large volumes and reflect single extracts.

2.3 Hydrogen isotope analyses and data reduction

Biphytane $^2H/^1H$ ratios were analyzed by gas chromatography pyrolysis isotope ratio mass spectrometry (GC-P-IRMS) on a GC IsoLink II IRMS System (Thermo Scientific), consisting of a Trace 1310 GC fitted with a programmable temperature vaporization (PTV) injector and either a 30 m ZB5HT column (i.d. = 0.25 mm, 0.25 µm, Phenomenex, Torrance, CA, USA) or a 60 m DB1 column (i.d. = 0.25 mm, 0.25 µm, Agilent, Santa Clara, CA, USA), ConFlo IV interface, and 253 Plus mass spectrometer (Thermo Scientific). Sample runs using the ZB5HT column used a fast ramp of the PTV to 400°C for sample transfer to the GC column and initial hold of the column at 60°C for 2 min, the GC oven was ramped to 350°C over the course of 14.5 min at a rate of 20°C /min, followed by an isothermal hold at 350°C for 7 minutes during which all biphytanes eluted (see Figure S1). Sample runs using the DB1 column used a fast ramp of the PTV to 330°C for sample transfer to the GC column and initial hold of the column at 60°C for 2 min, the GC oven was ramped to 220°C over the course of 7 min at a rate of 22°C /min, then to 330°C over the course of 14 min at a rate of 8°C /min, followed by an isothermal hold at 330°C for 20 minutes during which all biphytanes eluted.

All $^2H/^1H$ ratios are reported in delta notation (δ^2H) in permil (‰) units relative to the international seawater standard on the VSMOW-SLAP (Vienna Standard Mean Ocean Water, Standard Light Antarctic Precipitation) scale. All $^2H/^1H$ fractionation factors are reported in epsilon notation ($^2\varepsilon$) in permil (‰). All peak amplitudes are reported in volts (V) and refer to the amplitude of the *m/z* 2 measurement which has an operational amplifier with a 10^9 Ω resistor and thus reflects nA currents. Values of δ^2H were first determined relative to H_2 reference gas (δ^2H_{raw}), and then calibrated externally using a standard *n*-alkane mixture (A6, containing C_{15} through C_{30} *n*-alkanes spanning from -9 to -263 ‰ vs. VSMOW; A. Schimmelmann, Indiana University). The A6 standard was combined with a C_{36} *n*-alkane (nC_{36}, -259.2 ‰ vs. VSMOW; A. Schimmelmann, Indiana University) and measured at regular intervals at different concentrations. The BP hydrogen isotope calibration was performed in R based on 2195 compound-specific measurements from the A6 standard with peak amplitudes from 0.80 to 36 V (*m/z* 2) using the packages *isoreader* (v 1.3.0, (Kopf et al., 2021) and *isoprocessor* (v 0.6.11) available at github.com/isoverse. To correct for offset, scale compression and the peak-size effect inherent in δ^2H measurements (Liu et al., 2022), the following multivariate linear regression was inverted and applied to all standards and samples to determine δ^2H_{cal}:

$$\delta^2H_{raw} = \beta_0 + \beta_1 \cdot \delta^2H_{cal} + \beta_2 \cdot A + \beta_3 \cdot \delta^2H_{cal} \cdot \sqrt{A} \quad \text{(Eq. 1)}$$

where A signifies peak amplitude (*m/z* 2), and δ^2H_{cal} is the actual H-isotope composition of the analytes (known values for standard compounds; calibrated values for target compounds after inversion). The overall RMSE of calibration was 4.9‰ and residuals showed a random distribution (Figure S2, Panel 4), whereas other simpler regression models had substantially larger errors and showed systematic trends in their residuals (for a comparison of several different regression

models see Figure S2). To assess the uncertainty introduced by sample matrix and low signal-to-noise ratios, each biphytane peak was integrated multiple times in the Isodat software (v 3.0, Thermo Scientific), with manual background correction set before and after the eluting analyte peak. This analysis suggested integration errors to be negligible. Finally, to accurately assess peak-size dependent analytical uncertainty, the *n*-C_{36} standard was analyzed throughout in combination with the A6 standard because of its similar retention time to the biphytanes (elutes between BP-0 and BP-1). It was purposefully excluded from the calibration (Eq. 1) and was instead used to estimate the analytical error of the biphytane H isotope measurements after calibration using a local polynomial regression fit across all 73 *n*-C_{36} measurements spanning peak amplitudes from 0.06 to 27 V (*m/z* 2). This provided realistic peak-size adjusted error estimates of the calibrated measurements (σ_{cal}) with steep increases in the observed error at low peak amplitudes stepping from 3.9‰ at analyte peak amplitudes of 5V to 14‰ at 2V and 34‰ at 1V (Figure S3).

Calibrated δ^2H values for the biphytanes were corrected for the H added during hydrogenation of alkyl iodides. Assuming a similar isotope effect associated with the PtO_2-catalzyed reaction of H_2 and alkyl iodides as previously reported ($^2\varepsilon_{hydrog}$ = -721 ± 177 ‰; (Kaneko et al., 2011)), and the measured δ^2H value of the H_2 tank (δ^2H_{H2} = -64 ± 2 ‰; courtesy of Andrew Masterson, Northwestern University, IL, USA), the final corrected δ^2H values were calculated using the following equation:

$$\delta^2H_{cor} = \left(1 + \frac{2}{n_H}\right) \cdot \delta^2H_{cal} - \frac{2}{n_H} \cdot \left(\left({}^2\varepsilon_{hydrog} + 1\right) \cdot \left(\delta^2H_{H2} + 1\right) - 1\right) \quad \text{(Eq. 2)}$$

where n_H is the number of original H atoms in each alkyl chain. The total analytical uncertainty of the corrected δ^2H values was calculated using standard error propagation (Eq. 3) of the peak-size adjusted error estimates and hydrogenation correction assuming all errors to be uncorrelated. The hydrogenation correction ranged from 10.3 to 12.7 ‰ and increased analytical uncertainty by up to 1.9 ‰.

$$\sigma_{cor} = \sqrt{\left(\frac{\partial(\delta^2H_{cor})}{\partial(\delta^2H_{cal})} \cdot \sigma_{cal}\right)^2 + \left(\frac{\partial(\delta^2H_{cor})}{\partial(\delta^2H_{H2})} \cdot \sigma_{H2}\right)^2 + \left(\frac{\partial(\delta^2H_{cor})}{\partial({}^2\varepsilon_{hydrog})} \cdot \sigma_{hydrog}\right)^2} \quad \text{(Eq. 3)}$$

Hydrogen isotope analysis of growth medium water (δ^2H_{water}) was conducted with filter-sterilized media samples collected at the time of biomass sampling using an H-device (pyrolysis to H_2 gas) coupled to a dual-inlet IRMS (Thermo Delta Plus XL) and measured relative to a calibrated reference tank at 0.5‰ measurement uncertainty (1σ) (Taenzer et al., 2020). The resulting values of δ^2H were calibrated to the water isotope equivalent using standards of known composition. The hydrogen isotope fractionation between growth water and BP lipids ($^2\varepsilon_{L/W}$) was calculated according to Eq. 4:

$$^{2}\varepsilon_{L/W} = \left[\frac{(\,^{2}\delta_{cor}+1000)}{(\,^{2}\delta_{water}+1000)} - 1\right] \cdot 1000 \quad \text{(Eq. 4)}$$

Corrected bipythane δ^2H_{cor} values (Figure S1) and resulting $^{2}\varepsilon_{L/W}$ fractionation factors from sample and analytical replicates ($n \geq 4$ in all cases) were averaged for each experimental condition and are reported in Table 1 and visualized in Figure 1 (individual measurement values are in Table S1; Figure S1A). All averages are weighted means of individual measurements ($1/\sigma^2$ weights) to account for the amplitude-dependent range in uncertainties. The reported error estimate of each average is the larger of the standard deviation of all replicates vs. the propagated uncertainty from individual measurements. Changes in $^{2}\varepsilon_{L/W}$ per ring ($\Delta\varepsilon$/ring) were calculated as the average of isotope ratios for all combinations of ($\delta BP(x) - \delta BP(y < x)$)/(ring difference x-y) (Table 1).

2.4 Model Implementation

An isotope mass balance model to interpret the resulting $^{2}\varepsilon_{L/W}$ values was solved by implementing a simulated annealing routine (*simulannealbnd*) of the Matlab Global Optimization Toolbox (Matlab V2021b), using Monte Carlo resampling approaches (10^4 runs per trial). This approach minimizes the error cost function for multivariable optimization problems within prescribed bounds. It is agnostic to the presence of multiple local minima and is applicable to non-linear functions.

3. Results

Consistent with prior reports of the iGDGT distributions in *N. maritimus* SCM1 (Hurley et al., 2016; Elling et al., 2017), the relative abundances of BPs averaged 0.22:0.29:0.29:0.20 for BP-0, -1, -2, and -3, respectively (Figure S1C, Table 1), where BP-3 represents the cyclohexane-containing moiety of crenarchaeol. More details of the parent iGDGT compositions that yield these BP distributions, as well as the lipid responses to cultivation at steady state in chemostats, are available elsewhere (Hurley et al., 2016; Zhou et al., 2020).

The BPs were depleted in ^{2}H relative to growth water by as little as 257 ‰ (BP-3) to as much as 279 ‰ (BP-0) (Figure 1; Table 1). The abundance-weighted mean $^{2}\varepsilon_{L/W}$ value across all biphytanes from *N. maritimus* was -266 ± 9 ‰ (based on n = 73 total data points; Table 1, Table S1, Figure S1A). All growth conditions exhibit a systematic, ring-dependent change in the isotopic composition of their biphytanes (Figure 1; also see probability density distributions for each BP in Figure S1A) with decreasing $^{2}\varepsilon_{L/W}$ (enriched in ^{2}H) as the number of cyclic moieties increases. Though small, this effect appears to be real, as there is no systematic correlation between δ^2H residuals (*i.e.*, measurement accuracy) and peak intensities (Figure S1A) and changes in precision

are accounted for based on an internal standard (n-C_{36}) that has similar chromatographic retention to the biphytanes (Figure S3 and details in the Methods section). BPs -1, -2, and -3 were on average 5.3, 15, and 18 ‰ enriched in ^2H relative to the acyclic BP-0. Overall, each additional ring contributes a 6.4 ± 2.7 ‰ increase to biphytane δ^2H values across the full dataset. This pattern appears only minimally affected by differences in growth rate, with a positive, growth rate-dependent linear trend that is statistically insignificant (Figure 1).

4. Isotope flux-balance model

To generalize these findings and pave the way for future work with other archaea, we constructed an isotope flux-balance model (Figure 2) to explain both the magnitude of and patterns within the observed $^2\varepsilon_{L/W}$ values for *N. maritimus* (Figure 1). This analysis provides insight into the biochemical origins of archaeal $^2\varepsilon_{L/W}$ patterns and highlights their potential for proxy applications.

N. maritimus SCM1 grows autotrophically by the 3-hydroxypropionate/4-hydroxybutyrate (3HP/4HB) cycle using NH_4^+ as the electron donor (Könneke et al., 2014). It was chosen to explore potential impacts of growth rate variability on $^2\varepsilon_{L/W}$ patterns expressed by 3HP/4HB archaea, given the goal of developing an environmental proxy based on BPs of the globally ubiquitous, ammonia oxidizing Thaumarchaeota. Therefore, some sections of our isotope model and the ensuing discussion may not be applicable to all archaea; below we aim to distinguish between universal vs. metabolism-specific information.

4.1. Sources of hydrogen in archaeal lipid synthesis

In chemo(litho)autotrophic archaea, the hydrogen in lipid biosynthesis derives directly from intracellular water, from metabolic cofactors such as **NADPH**, or from inorganic cofactors such as ferredoxin (**Fd**; where the hydride (H^-) is abstracted from H_2O) (Figures 2 and 3; Figure S4 and S5). In heterotrophs there is also the potential for incorporation from organic substrate (e.g., glucose). NADPH is primarily derived from NADH via the electron transport chain. Minor additional amounts of NADPH may also be obtained from central metabolism (e.g., from isocitrate), but here we assume this source can be folded into the total NADPH pool. Given this complexity, we first examined in detail the origin of H in all biosynthetic steps to biphytanes and calculated stoichiometric scenarios – dependent on different source options – to serve as a framework for isotopic interpretations.

4.1.1 Synthesis of archaeal isoprenoids

In archaea, the synthesis of BP hydrocarbons proceeds as follows. Isopentenyl pyrophosphate (IPP) is synthesized from three units of acetyl CoA (Ac-CoA) using the mevalonate pathway (Figure 3, steps 1-6; (Chen et al., 1994; Koga and Morii, 2007; Hayakawa et al., 2018). Three units

of IPP and one of its isomer DMAPP together condense to yield geranylgeranyl diphosphate (GGPP, not shown; (Chen and Poulter, 1993)). The hydrogen in IPP derives both from the original acetate and from HMG-CoA reductase using NADPH as co-factor, while isomerization between IPP and DMAPP (Figure 3, step 6) also incorporates one H from water in place of one originally contributed by acetate. If the formation of DMAPP is limited to the minimum required to initiate isoprenoid condensation (1:3, DMAPP:IPP), only a single terminal H in the resulting GGPP retains the water signature. Additional water H (f_w) can be introduced either during IPP/DMAPP interconversion (Figure 3, step 6), and/or potentially during tautomerization of acetoacetyl-CoA (Figure 3, step 2), where if IPP-DMAPP isomerase is rapid relative to steps 7 and 8, then more water-derived H may be carried into the isoprenoid product. Thus, there is a range of stoichiometry possible for the fractional contribution of water-derived H, the consequences of which are elaborated below. Condensation of two di-*O*-geranylgeranyl glycerol phosphate (DGGGP) units into the membrane-spanning tetraether by the Tes enzyme eliminates two H, which would be of mixed water and acetate origin (Figure 3, step 8) (Zeng et al., 2022). Ring formation is catalyzed by GrsA and GrsB (Zeng et al., 2019) (Figure 3, step 9) and does not add any net hydrogen, but likely replaces some acetate-derived H with water-derived H. Saturation (Figure 3, step 10) is catalyzed by geranylgeranyl reductase (GGR). The electron donor for GGR in *N. maritimus* is not yet known, so for simplicity, we merge all electron-donor options into two choices: NADPH (Figure 3, step 10a) – i.e., we give GGR the signature of the NADPH pool used in steps 1-8; *or,* biosynthetic H is divided between NADPH and alternative oxidoreductases, namely those based on iron-sulfur clusters, e.g., ferredoxin (Fd), which we hypothesize could be the specific donor for GGR (Figure 3, step 10b).

Combining these ideas – high versus low extent of water exchange, and two potential types of hydride donors for GGR – yields four generalized permutations for archaeal isoprenoid biosynthesis, henceforth called Scenarios 1-4 (Table 2, Table S1).

4.1.2. Stoichiometric accounting: H sources in archaeal biphytanes

The four scenarios yield different budgets for the stoichiometry of biphytane H sources. Most of the 80 H atoms in the C_{40} alkyl chain of the acyclic biphytane (BP-0) are inherited from methyl-H of Ac-CoA (f_A, fractional contribution from Ac-CoA). Hydrides (H^-) are introduced from NADPH during biosynthesis of the mevalonate precursor to IPP ($f_{LipSynth\_NADPH}$), as well as during the final saturation of the alkyl chains by GGR in the scenarios where NADPH is the H-donor (f_{GGR_NADPH}); in both cases the paired protons (H^+) are obtained from water ($f_{LipSynth\_W}$, f_{GGR_W}). Alternatively, if Fd serves as the reductant to GGR, both H ultimately source from water (Isobe et al., 2014), but with potentially different isotope effects for the hydride and the proton. We therefore include a separate pool of H^- from Fd (f_{GGR_Fd}), while combining the paired H^+ with the water pool. Finally, for Scenarios 3 and 4, in which water is assumed to exchange freely with acetoacetyl-CoA during synthesis of IPP and DMAPP and IPP may rapidly isomerize, the model contains an exchangeable water fraction (f_x). The resulting stoichiometry of H sources to BP-0 is summarized in Table 2,

Table S1, and Figure S5. This accounting model is widely applicable across the archaea, i.e., it is not specific to the 3HP/4HB-pathway, and later can be utilized for other autotrophs, as well as heterotrophs (Figure 2B).

4.1.3. Sources of H in Ac-CoA generated autotrophically by the 3HP/4HB cycle

For any archaeon that grows as an autotroph, all three H of the Ac-CoA methyl group also derive originally from water. These H can be conceptualized as (*i*) direct incorporation of cellular water, or (*ii*) donation from reducing cofactors. The 3HP/4HB cycle generates Ac-CoA with a predicted ratio of 2:1 for direct water and cofactor hydrogens using reasonable biochemical assumptions for the mechanism of each step (see Figure S4). Thus, when there is no direct incorporation of H from organic substrates, the H assigned to Ac-CoA can be apportioned 0.67:0.33 among the water and NADPH pools of lipid biosynthesis (LipSynth). For example, re-distributing the 47 ⅓ H of Ac-CoA in Scenario 1 yields the following cumulative fractions: $f_{LipSynth\_W}$ = 0.83% + (0.6667)*59.17% = 40.28% and $f_{LipSynth\_NADPH}$ = 20% + (0.3333)*59.17% = 39.72%; see Table S1 for all proportions.

4.1.4. Summary budget and the impact of ring number

The stoichiometric budget for biphytane H sources in *N. maritimus* was further simplified for isotope flux balance analysis: water-derived H from lipid biosynthesis ($f_{\mathrm{LipSynth\_W}}$) was combined with GGR water protons ($f_{\mathrm{GGR\_W}}$) to yield total direct water H ($f_{*\mathrm{W}}$), and NADPH-derived hydrides from lipid biosynthesis ($f_{\mathrm{LipSynth\_NADPH}}$) were combined with hydrides associated with GGR ($f_{\mathrm{GGR\_NADPH}}$) to yield total NADPH sources ($f_{*\mathrm{NADPH}}$).

$$BP = \left(f_{LipSynth_W} + f_{GGR_W}\right) + \left(f_{LipSynth_{NADPH}} + f_{GGR_{NADPH}}\right) + f_{GGR_{Fd}} + f_x$$
$$= f_{*W} + f_{*NADPH} + f_{Fd} + f_x \qquad \text{(Eq. 5)}$$

Ring additions can be described by a formula that accounts for the proportional change in each H source (Eq. 6).

$$f_i^r = (f_i^0 + \Delta H_i \cdot r/n)/(1 - 2 \cdot r/n) \qquad \text{(Eq. 6)}$$

Here, the fractional contribution f_i^r of each H source i changes with the number of pentacyclic rings (r); ${f_i}^0$ is the fractional contribution of each source to BP-0; n is the number of H in BP-0 (= 80); and ΔH_i is the change in the number of hydrogens for each fraction per additional ring. The denominator reflects that for each additional pentacyclic ring, the molecule has 2 fewer H overall. The stoichiometry of adding a ring is not as straightforward as eliminating the incorporation of one H^- from GGR or Fd and one H^+ from water, where some substitution also is expected due to the mechanism of the ring cyclization reaction by radical *S*-adenosylmethionine proteins (Zeng et al., 2019), where one 1 H per ring is replaced (Pearson, 2019). For each f_i^r, the corresponding values of ΔH_i in *N. maritimus* are then as follows:

With NADPH as reductant:

For f_{GGR_NADPH}, $\Delta H_{GGR\_NADPH} = -1 \,/\, ring$

For f_{GGR_W}, $\Delta H_{GGR\_W} = -{}^{2}/_{3} \,/\, ring$

For $f_{LipSynth\_NADPH}$, $\Delta H_{LipSynth\_NADPH} = -{}^{1}/_{3} \,/\, ring$

With Fd as reductant:

For f_{GGR_Fd}, $\Delta H_{GGR\_Fd} = -1 \,/\, ring$

For f_{GGR_W}, $\Delta H_{GGR\_W} = -{}^{2}/_{3} \,/\, ring$

For $f_{LipSynth\_NADPH}$, $\Delta H_{LipSynth\_NADPH} = -{}^{1}/_{3} \,/\, ring$

The full stoichiometry of BP isomers -0, -1, -2, and -3 across Scenarios 1-4 is summarized in Table S1, which is calculated by combining Eq. 6 with Eq. 5 (*see* example in Figure S5). In all cases, having more rings is equivalent to having fractionally more water-derived H (Table 3). For scenarios in which Fd is modeled to be the electron donor to GGR, more rings also are somewhat counterintuitively associated with more H from NADPH (e.g., nearly 2% more for BP-3 in Scenario 2; Table 3), but these extra reducing equivalents are offset by having less H from Fd-hydride.

4.2. Hydrogen isotope flux balance model for archaeal biphytanes

Our quantitative model follows established approaches (e.g., Wijker et al., 2019). It divides the H isotope flux balance into two modules (Figure 2):

(1) *Cellular production* of NADH from the exogenous electron donor with H transfer to NADPH (transhydrogenation).

(2) *Biphytane synthesis* from water and the NADPH pool, plus the option to use Fd as an additional electron donor for GGR as explained in Section 4.1. For *N. maritimus* these are the only major sources of biphytane-H. For future analysis of heterotrophic archaea, this module also allows for incorporation of H directly from assimilated, rather than catabolized, organic substrates (not used for *N. maritimus*).

The H fluxes for *Biphytane synthesis* are set using the biosynthetic sources (Eq. 5). Solving the associated isotope budget for biphytane synthesis requires an estimate of the $^{2}H/^{1}H$ ratio of the NADPH pool, which is used throughout the cell and can have a variable isotope ratio depending on supply:demand, i.e., growth efficiency (Wijker et al., 2019). This necessitates the separate *Cellular production* module in which the pool of NADPH can vary. In ammonia-oxidizing (autotrophic) archaea, the only presumed source of NADPH is through an (as-yet unidentified) transhydrogenation reaction with NADH (Figure 2A) generated by the electron transport chain during ammonia oxidation (Walker et al., 2010). In heterotrophs, the sources of NADPH, and

therefore the potential effects on $^2H/^1H$ ratios of the NADPH pool, are more complex due to additional catabolic fluxes from organic precursors (Zhang et al., 2009; Wijker et al., 2019), which can also differ substantially between archaea and bacteria (Bräsen et al., 2014).

4.2.1. Cellular production module – Determining flux and isotope balance for NADPH

To allow for growth-rate dependent effects, this module permits reducing power (f_E, exogenous electron source) to be recycled as a leakage flux, f_L (Eq. 7). In a slight modification of the approach of Wijker et al. (2019), we symbolize this not as excess NADPH production, but rather an excess of electrons cycling through the NADH↔NAD$^+$ pool. Thus f_N, the production of NADPH co-factors from transhydrogenation of NADH, has a high fractional demand on f_E when the NADH supply (ammonia oxidation rate) is slow.

Mass balance, "*Cell*" module: $$f_E \equiv 1 = f_N + f_L \quad \text{(Eq. 7)}$$

The unused reducing power, or leakage, is modeled as a function of the energy available to the cell according to a parameterization factor λ. Both a slow growth rate (high T_D) and a low value of λ (highly efficient cell) decrease f_L. The cell is thus growing with maximum efficiency ($f_L \rightarrow 0$) at the slowest, most energy-starved doubling time (T_{D_max}; where $X_{TD} = 1$) (Eq. 8, 9).

Unused reducing power: $$f_L = \lambda(1 - X_{TD}) \quad \text{(Eq. 8)}$$

Growth rate dependence of f_L: $$X_{Td} = \frac{T_D - T_{D\text{-min}}}{T_{D\text{-max}} - T_{D\text{-min}}};\ f_L \downarrow \text{ as } T_D \uparrow \text{ and/or } \lambda \downarrow \quad \text{(Eq. 9)}$$

Combining these equations yields the isotope balance for NADPH production in ammonium oxidizing archaea, where all f_i are fractional fluxes and all R_i are $^2H/^1H$ ratios (Eq. 10, 11). Here, the $^2H/^1H$ ratio of NADPH is controlled by the fractionation relative to the electron donor pool (α_E, presumed to yield incoming NADH offset from R_W), in combination with the fractionation associated with the unknown transhydrogenation process (α_{TH}). The magnitude of R_{NADPH} is thus offset from R_{NADH} by a constant ($R_{NADPH} = \alpha_{TH} R_{NADH}$) and R_{NADH} varies as a function of f_N; see Figure S6. Note that these equations for cellular production of NAPDH are not universal and would require metabolism-specific modifications if used for other autotrophs or heterotrophs, whereas the biphytane synthesis module is generalizable.

Isotope balance, "*Cellular production*" module: $$R_{NADH} = \alpha_E R_W / (\alpha_{TH} + \lambda(1 - X_{TD})(1 - \alpha_{TH})) \quad \text{(Eq. 10)}$$

Then substitute (see Figure S6):

$$R_{NADPH} = \alpha_{TH} R_{NADH} = \alpha_{TH}\alpha_E R_W / (\alpha_{TH} + \lambda(1 - X_{TD})(1 - \alpha_{TH})) \quad \text{Eq. 11)}$$

4.2.2. Biphytane synthesis module – Determining flux and isotope balance for BPs

The value of R_{NADPH} (Eq. 11) is needed to calculate R_{BP} in the *Biphytane synthesis* module (Figure 2B, lower half). We presume all water protons are governed by a common KIE (α_W) and that all NADPH hydride sources have a single isotope effect α_{NADPH}. The alternate source of GGR reductants is symbolized by ferredoxin (f_{Fd}), with a potentially different isotope effect, α_{Fd}. To allow for isomerization-related exchange of water protons, we include the variable f_x ("exchange") with isotope effect α_x. The direct substrate flux, γ, would transmit unfractionated H directly from substrate to BPs; it is included to accommodate future modeling of heterotrophic taxa. The mass balance for biphytane synthesis is given by combining Eq. 5 with the γ term, which then yields the full isotope balance:

Isotope balance, "*Biphytane synthesis*" module:

$$R_{BP} = (1-\gamma)[(f_{*W}\alpha_W + f_x\alpha_x + f_{Fd}\alpha_{Fd})R_W + f_{*NADPH}\alpha_{NADPH}R_{NADPH}] + \gamma R_S \quad \text{(Eq. 12)}$$

Substitute Eq. 11 to obtain the isotope ratios of BPs:

$$R_{BP} = (1-\gamma)\left[f_{*W}\alpha_W + f_x\alpha_x + f_{Fd}\alpha_{Fd} + \frac{f_{*NADPH}\alpha_{NADPH}\alpha_E\alpha_{TH}}{\alpha_{TH}+L(1-X_{TD})(1-\alpha_{TH})}\right]R_W + \gamma R_S \quad \text{(Eq. 13)}$$

While Eq. 13 may describe the values and patterns for the $^2H/^1H$ ratios of biphytanes, it contains eight unknowns: γ, λ, and all six isotope effects, α_i. The problem is reducible, however, through a combination of supported assumptions, and by having data for multiple biphytanes, each at several different growth rates. These controlled variants impart predictable changes to the stoichiometric fractions, f_i, yet the corresponding values of R_{BP} must be satisfied using a single set of KIEs, α_i, unique to the organism. Additionally, the model must account for the observation that cyclopentane rings increase the $^2H/^1H$ ratio by > 6 ‰ ring^{-1} in response to shifts among the fractional hydrogen sources (Table 3). Cyclopentane rings are formed as an alternative to saturation by GGR, and therefore it may be informative to view the pattern from the opposite perspective: every GGR-mediated reduction ($H^- + H^+$) decreases $^2\varepsilon_{L/W}$ by -6.4 ‰ for a ~ 2/80 increase in total H budget. Thus, the net process of electron donation must have a negative KIE:

roughly -260‰ (= -6.4 ‰ ÷ 2/80) averaged across both the hydride and the proton. This is consistent with the overall $^{2}\varepsilon_{L/W}$ expressed for these organisms. It further indicates that the KIE associated with hydride donation is large, given prior assertions that the KIE of water incorporation is relatively small (Zhang et al., 2009; Wijker et al., 2019). Thus, we implemented a Monte-Carlo resampling approach to estimate all values of α_i and examine the results in the context of these data patterns. The respective scenarios and solutions are outlined below.

4.2.3. Model solutions, N. maritimus – Scenario 1: NADPH, no ferredoxin

In *N. maritimus*, γ is zero, reducing the problem to seven unknowns. Data for the four BPs and three growth conditions ($T_{D\text{-}min}$ and $T_{D\text{-}max}$ assumed to be 20 h and 120 hr; (Könneke et al., 2005; Santoro and Casciotti, 2011)) were modeled as follows.

Scenario 1: $f_x = 0, f_{Fd} = 0$; i.e., no extra water exchange and NADPH is the only H^- source.

$\lambda < 0.5$	electron donor flux is up to 50% leaky
$\alpha_W > 0.5$; $\alpha_W = 0.9$	water isotope effects may be moderate or small
$\alpha_{TH} = 0.01\text{-}1.0$	electron donor isotope effects may be large
$\alpha_E \bullet \alpha_{NADPH} = 0.669$	see Scenario 2 for details

While setting $f_{Fd} = 0$ can reproduce the relative patterning of $^{2}\varepsilon_{L/W}$ values for BPs of different ring numbers, i.e., BP-0 < … < BP-3, no implementation of this scenario can produce a large enough difference to match the data. Scenario 1 yields a maximum +3.1 ‰ ring^{-1} at the limit of $\alpha_{TH} = 0.01$, and this value yields too large a growth-rate effect (>> 0.2 ‰ hr^{-1}) due to the interdependence of α_{TH} and λ (Eq. 13). Conversely, at the correct growth-rate effect, the per-ring difference is no larger than +1.2 ‰ ring^{-1}. All attempts to adjust individual parameters failed to fix this deficiency, indicating Scenario 1 is oversimplified.

4.2.4. Model solutions, N. maritimus – Scenario 2: ferredoxin as reductant for GGR

If *N. maritimus* uses Fd as the H^- source for GGR, this not only alters the stoichiometric proportions of f_{*W}, f_{*NADPH}, and f_{Fd} for biosynthesis (Table 2), it also affects the proportional changes in these flux ratios at variable BP ring numbers (Table 3). This scenario can fully mimic the data and therefore was explored more completely.

Scenario 2: $f_x = 0$; Fd supplies H^- for GGR; NADPH supplies remaining lipid H^-.

Re-sampling range, initial conditions:

$\lambda < 1$	full range of leakiness permitted
$\alpha_W = 0.9$	constant (Zhang et al., 2009; Wijker et al., 2019)
α_{TH} and $\alpha_{Fd} = 0.01\text{-}1.0$	electron donor isotope effects may be large
$\alpha_E \bullet \alpha_{NADPH} = 0.01\text{-}1.0$	Case A, wide range
$\alpha_{NADPH} = 0.9, \Rightarrow \alpha_E = \alpha_E \bullet \alpha_{NADPH} \bullet 0.9^{-1}$	Case B, assumed $\alpha_{NADPH} = \alpha_W$

547
548 The value of α_W was constrained before solving for the other values of α_i. We initially set α_W to
549 float between 0.5-1.0, under the assumption that this value would be both moderate and variable.
550 However, all model runs consistently yielded a value of $\alpha_W \geq 0.9$ for the allowed solution space.
551 Based on this outcome and its agreement with prior literature (Zhang et al., 2009; Wijker et al.,
552 2019), we then fixed $\alpha_W = 0.9$, both here and retroactively in Scenario 1. Moderate changes in the
553 value assigned to α_W affect the absolute values of the model outcomes but do not affect the relative
554 patterns. Based on this apparently small isotope effect for α_W, we also chose to bypass any
555 scenarios that allowed isomerization-related exchange with water (f_x); i.e., we permanently set f_x
556 = 0 and eliminated Scenarios 3 and 4, as they seem inconsistent with the strong ^{2}H-depletion
557 indicated by the data.
558
559 Case A: The values of α_E and α_{NADPH} cannot be determined independently because their product
560 occurs in the numerator of a single term (Eq. 13). Acknowledging this, we first ran the model with
561 a wide allowed range (0.01-1.0) for the hydride transfer reactions α_{TH} and α_{Fd} and for the product,
562 $\alpha_E \bullet \alpha_{NADPH}$. This approach narrowly defined the optimal value of $\alpha_E \bullet \alpha_{NADPH}$ (0.669, $R^2 > 0.99$;
563 Table 4, Figure S6B) regardless of the values of the other parameters. Case B: As an alternative,
564 we defined $\alpha_{NADPH} = \alpha_W$. This is the implicit approach taken by Wijker et al. (2019) for the case
565 of bacterial fatty acids assuming NADPH hydrides are transferred to fatty acids directly (i.e.,
566 without explicit α_{NADPH}), but with the acknowledgement that this H may undergo water exchange.
567 When we adopt this alternative approach, α_E becomes uniquely 0.743 in the best-fit solution, given
568 that $\alpha_E \bullet \alpha_{NADPH}$ must remain 0.669 (Table 4).
569
570 Regardless of how the components of $\alpha_E \bullet \alpha_{NADPH}$ are defined, only a narrow range of solutions is
571 possible for α_{Fd}. The mean best-fit values are 0.14 ± 0.02 and 0.132 (with error < model bin step),
572 respectively, for the two cases. This is equivalent to ε_{Fd} = -860 to -868‰ (Figure 4A, Table 4),
573 which is as or more fractionating than current estimates for membrane-bound transhydrogenases
574 ($^2\varepsilon_{PntAB}$, -758 ‰; Jackson et al., 1999; Wijker et al., 2019).
575
576 In contrast, the solution for α_E (0.743) – or more robustly, the solution for the product $\alpha_E \bullet \alpha_{NADPH}$
577 (0.669) – is less fractionating than the estimate for α_{Fd} or bacterial PntAB. The process symbolized
578 by α_E, however, is not transhydrogenation, but rather the net KIE for transfer of H from the
579 inorganic electron donor by the electron transport chain, in which a membrane-bound electron
580 harvesting respiratory complex 1 (e.g., NDH1 a.k.a. Nuo (Walker et al., 2010)) is the likely source
581 of NADH production (Figure 2A). To our knowledge, specific characterization of the hydrogen
582 KIE for NDH1 has not been done; however, as NADH is the initial source of all reducing hydrides
583 in *N. maritimus*, we expect that the solution for α_E must be < α_W to yield strong ^{2}H-depletion in
584 lipids, and as a result also in net biomass.
585

586 The remaining unknowns are λ and α_{TH}, and again there is no unique solution (Eq. 13; Figure
587 S6C). However, every optimized combination of λ and α_{TH} must not only reproduce the ring-
588 dependence of the isotope composition of the individual BPs, but it must also show the observed
589 sensitivity (slope, ‰ hr^{-1}) of ${}^{2}\varepsilon_{L/W}$ to changes in growth rate. These relationships are visualized in
590 Figures 4B and 4C, in which the full solution space is indicated with black lines, but the permitted
591 solutions are defined by the regions over which the parameters yield both δ^2H values and growth-
592 rate slopes within error of the data (horizontal shaded areas). Exploration of this solution space
593 indicated the value of α_{TH} likely falls within the range of prior reports for soluble (sTH, $\alpha = 0.566$;
594 (Wijker et al., 2019)) and/or membrane bound (PntAB, maximum fractionation endmember $\alpha =$
595 0.222; (Jackson et al., 1999; Wijker et al., 2019)) transhydrogenases, and it makes little difference
596 to the model outcome if α_{TH} is constrained to any value between 0.222 to 0.566 (Table 4; see also
597 Figure S6C).
598
599 To further understand these results, a sensitivity analysis was performed by analyzing Eq. 13 for
600 its response to individual variables, while holding the others constant at the best fit predictions
601 (Figure 4). Among all the variables, the ^2H composition of BPs is most sensitive to α_{Fd}. Notably,
602 it also is more sensitive to λ than it is to α_{TH}, particularly to satisfy the requirement of minimal
603 sensitivity to growth rate. This sensitivity helps to further predict the likely value of α_{TH}. For
604 example, if λ is set to 0.04, the data are satisfied only by values of α_{TH} between 0.31 to 0.57, i.e.,
605 more similar to sTH than PntAB (Figure 4B). Alternatively, if α_{TH} is set to the mid-point (0.39),
606 the growth-rate slope limits λ to between 0.03 to 0.05. In comparison, the full model space allows
607 solutions for λ between 0.01 and 0.06.
608
609 Regardless, any reasonable estimate for α_{TH} implies the value of λ must be small, which is
610 consistent with the observation that ${}^{2}\varepsilon_{L/W}$ of *N. maritimus* biphytanes responds insignificantly to
611 changes in cell growth rate. Such a result also agrees with the concept that Archaea are optimized
612 for energy-limited conditions (Valentine, 2007), implying that nearly all reducing power (NADH
613 derived from the e^- donor) is allocated to obligatory cellular needs. At the estimate of $\lambda = 0.04$ and
614 a mid-point of $T_D = 56$ hr, the value of $f_N = 98\%$ (Eq. 8, 9), i.e., only 2% of produced NADH is
615 lost (f_L). A 98% value for f_N represents the electron flux that is harvested from NADH into the
616 NADPH pool and obligately dedicated to the full suite of cellular metabolic fates, only part of
617 which is lipid synthesis. If this conceptual framework is robust, it would be difficult to change the
618 isotopic composition of NADPH due to effects around the f_N vs. f_L branch point (Hayes, 2001),
619 and ${}^{2}\varepsilon_{L/W}$ should be very insensitive to growth rate, not only in AOA, but potentially in all
620 autotrophic archaea.
621
622 The final estimated solutions for Scenario 2 (Table 4) reproduce the three major features of the
623 ${}^{2}\varepsilon_{L/W}$ data for *N. maritimus* biphytanes: (*i*) highly ^2H-depleted absolute values, (*ii*) relative
624 insensitivity to changes in growth rate, and (*iii*) the increase in isotope ratio with ring number.

Specifically, the consensus model yields an increase of +6.7 ‰ per ring, compared to the +6.4 ‰ per ring observed for the data, and yields a small positive slope of $^{2}\varepsilon_{L/W}$ versus T_D (Figure 5). Most of the ring-associated increase is attributed to the large KIE of the Fd reductant, while the relatively shallow growth-rate slope reflects the small value of λ, which likely reflects inflexible physiological fluxes in *N. maritimus*.

5. Discussion

The motivation for this work was to investigate the potential of $^{2}H/^{1}H$ ratios of archaeal lipids as archives of past environments, ecologies, or physiologies. In sharp contrast to the > 600 ‰ range of values observed across the bacteria, to-date the archaea stand out for their apparently narrow span of $^{2}\varepsilon_{L/W}$ values. This is somewhat unexpected, given the diversity of species, growth substrates, and metabolic strategies among the archaeal taxa studied to date (e.g., Kaneko et al., 2011; Wu et al., 2020). Archaeal lipids appear always to be ^{2}H-depleted relative to growth water and sit at the lower end of the range previously reported for bacterial fatty acids (Sessions et al., 2002; Valentine et al., 2004; Campbell et al., 2009; Zhang et al., 2009; Heinzelmann et al., 2015; Osburn et al., 2016; Leavitt et al., 2016; Leavitt et al., 2016; Leavitt et al., 2017).

Our results for *N. maritimus* show that BPs were generally more ^{2}H-depleted (-257 ‰ for BP-3 to 279 ‰ for BP-0) than the range of $^{2}\varepsilon_{L/W}$ values from the heterotrophic and halophilic archaeon *Haloarcula marismortui*, which yielded archaeol/water fractionations of -103 to -228 ‰ (Dirghangi and Pagani, 2013), and batch cultures of hyperthermoacidophilic *Sulfolobus* spp. (Kaneko et al., 2011; Lengger et al., 2021), from which BPs (raw, not relative to water) and GDGTs/water were fractionated by -207 to -257 ‰ and *ca*. -180 ‰, respectively. The values we observe for *N. maritimus* are similar to the range from *Methanosarcina barkerii*, which yielded fractionations from -204 to -322 ‰ for phytanes/water, depending on methanogenesis substrate (Wu et al., 2020). *N. maritimus* expresses simple patterns of $^{2}\varepsilon_{L/W}$ values, where the dominant feature is a dependence on the number of rings, with the most ^{2}H-depleted values in BP-0 and the least depleted in BP-3 (Figure 1). Mean total assemblage values of $^{2}\varepsilon_{L/W}$ show little sensitivity to changes in growth rate as promoted by different fluxes of electron donor, especially when compared to the fatty acids of bacteria grown with similar strategies (Kopf, 2015; Kopf et al., 2015; Leavitt et al., 2019) The model developed above (Section 4) explored how these patterns can help distinguish the H sources for BP biosynthesis and enabled estimation of the KIEs for the various enzymatic steps.

The key attributes required by the model solution (Scenario 2) are a highly fractionating value of ferredoxin-derived hydrides (α_{Fd}), a relatively less-fractionating value for NADH-NADPH transhydrogenation processes (α_{TH}), and an aggregated electron donor flux (i.e., $\alpha_{NADPH} \bullet \alpha_{NADPH}$)

somewhat less fractionating than α_{TH}. The minimal growth rate sensitivity implies that *N. maritimus* undergoes almost no change in cellular flux balance, regardless of having relatively fast or slow growth. This implicates a constant baseline δ^2H signature as a feature of a relatively imperturbable central energy metabolism. Stepping beyond this experimental and model framework, we now look toward physiological inferences and paleoenvironmental applications.

5.1. Biochemical drivers of $^2\varepsilon_{L/W}$ patterns

5.1.1 Sources of cofactor hydrogen for lipid synthesis in 3HP/4HB Archaea

N. maritimus is an obligate chemoautotroph that utilizes the 3HP/4HB pathway for carbon fixation (Kim et al., 2016; Bayer et al., 2019, Könneke et al., 2014). Because all biphytane-bound H in the present experiments is strictly biosynthetic, rather than assimilated as part of an organic substrate, the observed differences in $^2\varepsilon_{L/W}$ values between individual BPs (Figure 1) must be primarily due to different KIEs associated with the hydride transfer reactions that recharge intracellular electron donors. As such, the patterns we observed here may be expressed differently in heterotrophic archaea or during mixotrophic growth.

In the model framework developed here, the overall mean value for $^2\varepsilon_{L/W}$ in *N. maritimus* reflects primarily the expression of α_E (0.743; equivalent to ~ -260 ‰), while the ring-based differences and growth-rate effects are controlled by the downstream flux balances and KIEs (λ, α_{TH}, α_{NADPH}, α_{Fd}). This implies that $^2\varepsilon_{L/W}$ likely would or should be expressed differently in heterotrophic archaea. This may help to explain why our results are similar, yet not equal, to prior data from *Haloarchula marismortui* and *Sulfolobus spp.* (Kaneko et al., 2011; Dirghangi and Pagani, 2013); these prior data also were not obtained on steady-state cultures, which may be an additional factor contributing to the observed differences. The only major catabolic enzyme in *N. maritimus* is isocitrate dehydrogenase (ICT) in the TCA cycle, which we expect to be minimally expressed (Könneke et al., 2014). However, in a range of heterotrophic aerobic archaea (e.g., *Sulfolobus* species), not only this step, but more importantly glucose dehydrogenase from the Entner-Doudoroff pathway should be a major NADPH contributor (Nunn et al., 2010; Bräsen et al., 2014), potentially with an impact on the final $^2\varepsilon_{L/W}$ signature.

The most definitive result of our modeling approach (Section 4) is the prediction of a highly fractionating KIE (α_{Fd}) for the e^- donor for GGR during saturation of DGGGP, which stands separate from the above caveats. The *in vivo* electron donor for GGR is not yet known in *N. maritimus*, but our inference of a specific role for ferredoxin-mediated reduction agrees with other reports. To date there is no direct evidence that NADPH is used as the hydride donor for GGR in archaea (Murakami et al., 2007; Sato et al., 2008). In contrast, observations from cyanobacteria and plants (*Synechocystis* and *Arabidopsis* spp.) show GGR was directly reduced by NADPH (Addlesee et al., 1996; Keller et al., 1998).

This raises the question: what is the major source of hydride to BP's in *N. maritimus*? The most likely candidate appears to be ferredoxin-$NADP^+$ reductase (FNR; Figure 2A), which is highly conserved among both the pelagic marine and the terrestrial AOAs – though may be absent in the non-AOA Thaumarchaeota (Ren et al., 2019). This distribution may indicate reduction of Fd by NADPH is common in some archaea (Aliverti et al., 2008), and suggests Fd may be a common or even the dominant hydride donor in *N. maritimus*. More convincing evidence for the role of Fd in isoprenyl chain saturation (Figure 3, step 10b) comes from the heterologous expression of *Methanosarcina acetivorans* GGR in *E. coli*, where saturation of DGGGP only occurred when a functional Fd from *M. acetivorans* was also provided (Isobe *et al.*, 2014). Although in an analogous experiment on *S. acidocaldarius*, GGR was active without including a native Fd, the authors note *E. coli* Fd was present and suggested it may have played a role. Alternatively, however, it appears that some archaeal GGRs may utilize a NADH-flavin cofactor process for hydride transfer: *in vitro* studies of GGRs from thermoacidophiles *Sulfolobus acidocaldarius* and *Thermoplasma acidophilum* implicated this mechanism instead (Nishimura and Eguchi, 2006; Sasaki et al., 2011).

Although we specify the GGR reductant is NADPH-Fd (FNR; Figure 2), rather than NADH-flavin, more work is needed to distinguish these two options. Our choice to invoke the former is based on two arguments. First, it appears that ferredoxin-dependent and flavin-NAD complexes may be favored in chemo(litho)autotrophs (Buckel and Thauer, 2018; Boyd et al., 2020). Second, there is evidence that Fd co-factors could carry very large isotope effects into the donated H^- pool. This feature is a requirement to generate a relatively large (6.4 ‰) per-ring shift in ${}^2\varepsilon_{L/W}$. The strong ^{2}H-depletion (α_{Fd} = 0.13 to 0.14; -860 to -870 ‰; Table 4) we estimate for the GGR reductant may be broadly consistent with prior estimates that fractionation of hydride donors to Fd and $NADP^+$ during photosynthesis in cyanobacteria are on the order of α = 0.43 relative to water (Luo et al., 1991), although this still falls considerably short of our predicted KIE for Fd. More promisingly, direct rate assays for the two isotopes (k_{1H}/k_{2H}) using purified *Anabena sp.* FNR show values from 5.7 to 6.4 (4,700 to 5,400‰) due to hydrogen tunneling (Peregrina et al., 2010; Sánchez-Azqueta et al., 2014). In general, these reports indicate large isotope fractionations during hydride transfers that involve iron-sulfur clusters. Given the wide distribution of FNR in marine AOA, we therefore suggest that it is both the most likely donor for GGR (thereby resembling *M. acetivorans*), and that its KIE *in vivo* is likely to be highly fractionating. Regardless of specific carrier, however, our model provides tight constraints on the $^2H/^1H$ signature of the GGR donor.

Regardless of any inferences about the hydride sources to GGR, synthesis of GDGTs also requires hydrides donated directly from NADPH, both during synthesis of acetyl-CoA (Figure S4) and later, during polyisoprene synthesis to yield DGGGP (Figure 3, steps 1-7). The core catabolic pathway of ammonia oxidation in *N. maritimus* and other AOAs, however, likely generates NADH via ferredoxin or FAD-dependent oxidoreductases interacting with Nuo = NDH1 (NADH:ubiquinone oxidoreductase) rather than NADPH (Walker et al., 2010; Qin et al., 2018; Shafiee et al., 2022). It is unclear if Nuo can generate NADPH in AOAs. In case it cannot, this

necessitates *N. maritimus* to produce NADPH for anabolism by other means (Spaans et al., 2015) such as via a yet unidentified transhydrogenase (as assumed in our metabolic model). A better understanding of the precise mechanism(s) by which *N. maritimus* interconverts NADH↔NADPH, or how it generates NADPH directly during catabolism, is central to interpreting the $^{2}\varepsilon_{L/W}$ signatures encoded in its lipids. Similarly, these sources of lipid H will need to be identified in all BP and GDGT synthesizing archaea in order to understand their lipid-H isotope signatures.

In bacteria, the biosynthetic NADPH pool is regenerated by transhydrogenation from NADH, and thus sources its reducing power directly from the primary supply generated by the electron transport chain (Sauer et al., 2004; Fuhrer and Sauer, 2009). In most bacteria this process is catalyzed by transhydrogenase (TH) enzymes that transfer the hydride (H^-) between NADH and $NADP^+$ as needed to replenish deficits as NADPH hydrides are consumed during anabolism (biosynthesis) (Sauer et al., 2004). The hydride transfer reaction by bacterial TH enzymes are associated with a strong ^{2}H discrimination (ε_{TH} = -778 ‰ to -434 ‰; (Jackson et al., 1999; Wijker et al., 2019)). While homologues of bacterial THs are seen in some methanogens, they are otherwise rare in Archaea (c.f. (Buckel and Thauer, 2013, 2018; Leavitt et al., 2016; Poudel et al., 2018). Consistent with this rarity, we were unable to find homologues to common bacterial (e.g., *E. coli* or *D. alaskensis*) soluble or membrane associated transhydrogenases in the *N. maritimus* genome (Table S2). *N. maritimus*, like other archaea, does encode other mechanisms to balance their intracellular redox budgets (Spaans et al., 2015; Boyd et al., 2020) and all NADPH producing enzymes annotated in the *N. maritimus* genome are summarized in Table S2. The main NADPH sources not associated with central carbon metabolism include a cytosolic NADP+-reducing hydrogenase (SH; Nmari_0253, Nmar_0267, Nmar_1389), and the aforementioned ferredoxin:NADP+ oxidoreductase (FNR; Nmar_0672). Sources of NADPH coupled to the TCA cycle is the IDH (Nmar_1069, Nmar_1379) mentioned above, and coupled to the non-phosphorylating Entner Doudoroff pathway is a NADP+ glyceraldehyde dehydrogenase (Nmari_1608). Given the lack of transhydrogenase identified in the SCM1 genome, and the other sources, the main NADPH producing mechanism of note is FNR, with its predicted large fractionation.

From the isotopic perspective, our $^{2}\varepsilon_{L/W}$ data appear to be consistent with the picture that has emerged from bacterial transhydrogenases. That is, the known KIE associated with bacterial NADPH/NADH hydride transfer is strongly fractionating (Table 4), but is not as ^{2}H-depleted as hydrides supplied by Fd via FNR. Regardless, our model is not very sensitive to the value chosen for α_{TH}, since it simply couples a stronger fractionation (smaller assigned α_{TH}) to a lower degree of "leakiness" (smaller λ) or the converse (less fractionating α_{TH} with larger λ) to achieve equal goodness of fit (Figure 5). It is therefore more informative to note that this approach places hard constraints on the maximum value of λ and indicates there are no permitted solutions that enable significant energy waste (lost NADH, f_L) in *N. maritimus*. It also appears unlikely that the process

identified here (generation of f_N with α_{TH}) is somehow the same as that symbolized by the f_{Fd} contribution, i.e., the lack of overlap between estimates for α_{TH} and α_{Fd} indicates two unique sources of reducing hydrides are required, even if in the present configuration we have identified them incorrectly.

5.1.2. Interpreting metabolic limits on $^2\varepsilon_{L/W}$ values

In the framework set forth by Wijker et al. (2019) for bacteria, *N. maritimus* would be operating near the NADPH imbalance flux approaching -100% (see Wijker et al. (2019) Figure 3). Although the notation between our model and theirs is different, our best fit estimate for $\lambda = 0.04$ (range 0.01 to 0.06; Table 4) equates to a balance around NADH where 98% of the electron flux is required for NADPH generation and only 2% is in "excess" for recycling or leakage. This places *N. maritimus* at -98% NADPH imbalance in the Wijker et al. (2019) reference frame (Figure 6).

The maximum H isotope fractionation for average BPs relative to water can be inferred from Figure 6 by extrapolating to -100% NADPH, yielding an intercept of -282 ‰. It remains unknown whether this also is a reasonable approximate minimum value for $^2\varepsilon_{L/W}$ for bacterial production, or whether the ~ 200‰ scatter in the vertical dimension in Figure 7 portends a similar range for the projected minima of diverse organisms. A possibility that requires further investigation is whether free energy differences, i.e., impacts on α_E, are primarily responsible for changes in $^2\varepsilon_{L/W}$ at a given NADPH imbalance (changes in the vertical), while changes in flux balance, growth rate, and overall energy demand set this imbalance. If so, more experiments at constant energy flux for organisms with distinct metabolisms will help define this space, and the outcome of inferred α_E may reflect thermodynamic properties of the experiments. Any potential contributions from equilibrium isotope exchange in various reaction steps also remain unknown. Such effects could be examined by cultivation at different temperatures, although likely with a different taxon (*N. maritimus* is grown isothermally at 28 °C). Thus, while we do not know how the observed $^2\varepsilon_{L/W}$ we observed at 28 °C relates to the maximum KIE of a unidirectional hydride (H^-) donation, or whether there is H^- isotopic exchange at equilibrium, we can infer that considerable kinetic expression is required (also justifying our exclusion of Scenarios 3 and 4 in the original model). Theoretical calculations of the equilibrium isotope effect (EIE) for an idealized isoprenoid vs. water yielded an estimate of -100 ‰, which was essentially insensitive to temperature over a range of 0 to 100 ºC (Wang et al., 2009). This is effectively the same as what we assigned empirically for the water KIE ($\alpha_W = 0.9$) and suggests the water-derived KIE component of BP biosynthesis will not respond to temperature variations. Together these examples imply that the $^2\varepsilon_{L/W}$ signals of Thaumarchaeota BPs are unlikely to be temperature-sensitive, in addition to their insensitivity to growth rate.

5.2. Applications

5.2.1 Calibrating biphytane $^2\varepsilon_{L/W}$ offsets for paleohydrology and paleoecology

Archaeal lipids may offer some unique advantages as H isotope proxies. The iGDGTs found in aquatic sediments are believed to derive predominantly from marine or lacustrine ammonia-oxidizing Thaumarchaeota living in the overlying water column (Powers *et al.*, 2010; Pearson and Ingalls, 2013, Schouten et al., 2013). This contrasts with leaf wax-derived *n*-alkanes, which can derive from a complex plant community, may have both terrestrial and aquatic sources, and production is seasonally-biased in some regions (Gao et al., 2011; Sachse et al., 2012; McFarlin et al., 2019). The larger diversity of $^2\varepsilon_{L/W}$ values expressed by *n*-alkanes reflects both the diversity of the local ecosystem and this source-transport signal (Sachse et al., 2012; Gao et al., 2014). In lacustrine bodies with minimal terrigenous overpriting, it may be possible to reconstruct the water δ^2H composition from archaeal biphytanes and an estimated constant $^2\varepsilon_{L/W}$ value, using either a mean value or individual BP-specific values. Tandem work on modern lake core-tops over a range of temperature regimes may provide an indication of the magnitude of any temperature effects, though it remains unknown whether this archaeal $^2\varepsilon_{L/W}$ offset is temperature sensitive (*see* section 5.1.2). Once calibrated, the reconstructed lake water record could be compared to estimated regional meteoric water δ^2H values obtained from co-deposited *n*-alkanes that reflect water available to the surrounding vegetation during the period of leaf synthesis (Tipple et al., 2013), potentially yielding insights to past changes in the hydrologic cycle or plant physiological effects that can be missing from the plant perspective (Sachse et al., 2012), and may help unpack diverse GDGT sources in some lacustrine systems when paired with C-isotopes (Sinninghe Damsté et al., 2022). In the marine environment, variation in the δ^2H value of ocean water is minimal, and a modern core-top calibration would serve to uniquely calibrate temperature signals independently from variations in source water. Both types of calibration efforts likely will be needed.

Variations in salinity have *ca.* 50 ‰ effects on the $^2\varepsilon_{L/W}$ values of alkenones from haptophyte algae (Schouten et al., 2006; van der Meer et al., 2015; Sachs et al., 2016). The mechanism by which salinity affects $^2\varepsilon_{L/W}$ values in haptophytes remains unclear, but it has been hypothesized that such effects may be restricted to photoautotrophs (Heinzelmann et al., 2015a). Differences in salinity and taxonomy produce different iGDGT assemblages among Thaumarchaeota (Elling et al., 2015; 2017), which would then yield differences between taxa in their bulk average $^2\varepsilon_{L/W}$ values to be consistent with the pattern of increasing $^2\varepsilon_{L/W}$ for BP-0…BP-3. However, estimates of the net effect of such changes based on variation in Ring Index suggests that the effect would be minimal (< 10 ‰), even between the very high Ring Index composition of *Nitrososphaera gargensis* (BP-0:1:2:3 ratio of 0.02:0.02:0.51:0.45; calculated by Elling and colleagues by assuming iGDGT-2 consists only of 2 x BP-1 (Elling et al., 2017)) vs. the BP distribution in *N. maritimus*. Thus, the taxonomic influence of iGDGT compositional changes on average $^2\varepsilon_{L/W}$ should be insignificant. Whether $^2\varepsilon_{L/W}$ values are influenced by salinity independently of changes in ring distribution requires further investigation. It may be likely that regional temperature calibrations would overwhelm any salinity effects or taxonomic community shifts in the evaluation of either lacustrine

or marine biphytane δ^2H proxies. For applications in lacustrine or riverine sediments, salinity is of no concern, but alternatively, proxies in these settings should be examined for potential pH effects.

Growth rates of natural microbial communities can vary spatially and temporally, depending on the availability of nutrients, electron donors and acceptors, temperature, and other environmental parameters. The conditions used in this work were designed to test a broad range of metabolic rates at controlled steady state. We anticipated that variations in energy budgets associated with fast and slow growth would yield heterogeneity of ${}^2\varepsilon_{L/W}$ values analogous to the differences in ${}^2\varepsilon_{L/W}$ values of bacteria grown aerobically on different hexoses (Wijker et al., 2019), or haptophyte algae grown at different rates by varying the temperature (Schouten et al., 2006) or nutrient supply (Sachs and Kawka, 2015). Instead, we observed a nearly zero growth rate effect on expression of ${}^2\varepsilon_{L/W}$ in *N. maritimus* despite using a 3-fold range of doubling time that is believed to encompass most of the natural conditions of marine AOA (e.g., (Santoro and Casciotti, 2011; Qin et al., 2014)). The direction of this response is the same as for haptophyte algae, with a decrease in ${}^2\varepsilon_{L/W}$ (i.e., greater fractionation) observed at faster growth rates, but with a magnitude significantly less than what was observed for lipids of algae grown in chemostats (Sachs and Kawka, 2015). Previous work on *Haloarcula marismortui* (a halophilic archaea) showed variations in ${}^2\varepsilon_{L/W}$ values up to 25 ‰ between fastest and slowest growth (T_D from 8 to 16 h; (Dirghangi and Pagani, 2013). However, because the halophile work was done in batch culture, these doubling times reflect non-constant growth rates and integrate across the culture's growth stages, making direct comparison to our steady-state experiments difficult. We suggest that the highest growth-rate sensitivity for ${}^2\varepsilon_{L/W}$ values of archaea likely would be expressed in cultures cultivated at maximum free energy (e.g., aerobically on simple sugars), and that studies in aerobic heterotrophs are necessary to confirm this endmember. Environmental conditions likely would be more constrained, and accordingly there should be less growth-rate variability in ${}^2\varepsilon_{L/W}$ for natural archaeal communities, and especially for those that are autotrophic like the ammonia-oxidizing Thaumarchaeota.

Collectively our data support the idea that a unifying feature of the archaea is the operation of maximally energy-efficient metabolisms (Valentine, 2007). This is reflected by highly fractionated lipid δ^2H values, which are consistent with an overall metabolic status of having just enough NADPH or other internal electron donor to meet cellular demand (Wijker et al., 2019). We would further suggest that the inability to shift ${}^2\varepsilon_{L/W}$ values off this minimum in *N. maritimus*, even when supplying electron donor at an increased rate, indicates the marine Thaumarchaeota have inherently stable internal fluxes that were selected for during their adaptation to extreme oligotrophy (Martens-Habbena et al., 2009). This would be consistent with supply-side control of the rate of archaeal metabolism (Amenabar et al., 2017). Unless growth temperature has a significant impact, marine and lacustrine autotrophic Thaumarchaeota will have reliably invariant ${}^2H/{}^1H$ fractionation regardless of growth rate, nutrient status, or differences in community composition, and the environmental expression of archaeal ${}^2\varepsilon_{L/W}$ should be more constant than for marine algae.

899

900 **5.2.2. Distinguishing iGDGT sources using stable isotope patterns of biphytanes**

901 Combining carbon and hydrogen isotope analyses of sedimentary biphytanes may provide a
902 powerful new means to disentangle sources and processes. In marine systems, compound
903 distributions and carbon isotopic measurements indicate sedimentary iGDGTs appear to be derived
904 mostly from local planktonic sources (Shah et al., 2008; Pearson et al., 2016; Zhang et al., 2016).
905 Easily detectable exceptions are cases where methane cycling has affected the $\delta^{13}C$ ratios and
906 iGDGT profiles of the sedimentary lipid pool (e.g., (Sinninghe Damsté et al., 2001; Wakeham et
907 al., 2003; Hoffmann-Sell et al., 2011; Zhang et al., 2011). However, the resolution of $\delta^{13}C$ isotope
908 ratio mass balance estimates is relatively coarse, and radiocarbon measurements can be logistically
909 difficult to acquire in sufficient numbers to yield definitive conclusions. There are many instances
910 of minor deviations in Ring Index (Zhang et al., 2016) or small but consistent differences between
911 $\delta^{13}C$ values of iGDGTs – particularly the notable ^{13}C offset of *ca*. 1 ‰ between iGDGT-0 and
912 crenarchaeol that occurs in many marine sediments (Pearson et al., 2016; Polik et al., 2018; Elling
913 et al., 2019) – that require better understanding. Whether these signals are simply noise (e.g., due
914 to sediment mixing or other factors), or whether they reflect systematic differences in sedimentary
915 sources, is critical to the interpretation of iGDGT proxies such as the widely applied TEX_{86} sea-
916 surface temperature proxy (Schouten et al., 2002). Such signals may be diagnosable through $\delta^{2}H$
917 analysis of individual BPs.

918

919 The capacity to produce cyclopentyl-ring containing iGDGTs is widely distributed among the
920 archaea (Zeng et al., 2019), but the cyclohexyl ring-containing iGDGT, crenarchaeol, is believed
921 to be unique to the Thaumarchaeota (Pearson and Ingalls, 2013; Schouten et al., 2013). The
922 iGDGTs in marine and lacustrine sediments therefore have the potential to integrate multiple
923 sources, such that even if the dominant source is export of planktonic AOA, there also may be
924 cases of significant input of benthic, soil-derived, or other allochthonous lipids. The distinctive
925 pattern in relative $^{2}\varepsilon_{L/W}$ values between BP chains of a single source could serve as an isotopic
926 fingerprint to identify the contribution of these multiple iGDGT sources to sedimentary archives.
927 BPs obtained from any sediment in which the archaeal lipids reflect a homogeneous community
928 growing in a common body of water should have equal $\delta^{13}C$ values (Hurley et al., 2019), as well
929 as predictable differences in $\delta^{2}H$ values that conform to the pattern BP-0 < BP-1 < BP-2 < BP-3.
930 Of these, the unique cyclohexane-containing BP-3 from crenarchaeol would serve as the anchor
931 point for the planktonic signal.

932

933 A further advantage of this dual-stable isotope approach is the ability to obtain both sets of
934 measurements (plus the overall iGDGT profile and the TEX_{86} ratio) from the same sample. This
935 subverts the challenges of other multi-proxy approaches that may require comparison of lipid
936 extracts to solid phases (e.g., elemental analyses for soil Al/Ti). Archaeal lipids from terrestrial
937 freshwater environments are likely to be more depleted in ^{2}H than those produced in seawater,
938 with a differential that increases with latitude. Similarly, $\delta^{13}C$ values of archaeal BPs from

continental sources may be either more negative or more variable than marine waters (Weijers et al., 2009; Lattaud et al., 2021). Dual C and H isotope patterns for BPs may prove particularly useful to diagnose terrestrial iGDGT inputs to marine sediments, thereby adding to the distribution metrics such as Ring Index, Methane Index, iGDGT-2/3 ratio, and other profiling strategies (Zhang et al., 2011, 2016; Taylor et al., 2013; Dunkley Jones et al., 2020) that currently are used to assess fidelity of the TEX_{86} index. Furthermore, the archaeal lipid-H proxy may be useful in tracking past climate through events such as the PETM in terrestrial records, and perhaps more recent shifts in the Plio-Plistocene and Holocene.

5.3 Summary

In this study we quantified the hydrogen isotope fractionation between growth water and lipids in a well-studied strain of the ubiquitous marine ammonium oxidizing archaea in response to different steady-state electron donor fluxes. We observed little sensitivity to growth rate and a consistent pattern in the ordering of isotope fractionation with biphytane ring number. These observations are captured well in a bio-isotopic model, despite limited literature available on the intracellular hydride and electron carriers in environmentally important archaea. From the model, it is clear chemoautotrophic archaea, such as *N. maritimus,* add hydrides to the isoprenoid chains of GDGTs from a strongly depleted intracellular reservoir of NADPH. Moreover, *N. maritimus* cells in particular operate at near constant NADPH deficit as compared to previously studied bacteria. We extend the recent modelling approach of Wijker et al. (2019) to the Domain Archaea, and propose this framework is universal to microorganisms. Further experimental work within the archaea, both in aerobic chemolithotrophs such as the AOAs, as well as in anaerobic chemolithotrophs and aerobic and anaerobic heterotrophs, is necessary to determine how universal the lipid-water fractionation response is in the Archaea. These and subsequent experimental studies will determine how useful archaeal lipid hydrogen isotopes will be for use in paleohydrology and paleoecology.

6. Acknowledgments

This research was supported by funding from: collaborative research grant NSF EAR #1928303 (WDL, SHK); the American Chemical Society PRF #57209-DNI2 (WDL, YW); Simons Foundation Award #623881(WDL); Swiss National Science Foundation P2BSP2_168716 (YW); NSF OCE-1843285 and 1702262 (AP); Dartmouth College via start-up funds (WDL); the University of Colorado Boulder via start-up funds and a seed grant to SHK; the Deutsche Forschungsgemeinschaft grant EL 898/2-1 (FJE). The authors thank M. Könneke for providing strain SCM1; B. Meade for discussions that improved this work; X. Feng for assistance with water H-isotope measurements; as well as the analytical contributions of the CU Boulder Earth Systems Stable Isotope Lab (CUBES-SIL) Core Facility (RRID:SCR_019300).

7. Data & Model availability: https://github.com/KopfLab/2022_leavitt_et_al.

7. References

Addlesee H. A., Gibson L. C., Jensen P. E. and Hunter C. N. (1996) Cloning, sequencing and functional assignment of the chlorophyll biosynthesis gene, chlP, of Synechocystis sp. PCC 6803. *FEBS letters* **389**, 126–130.

Aliverti A., Pandini V., Pennati A., de Rosa M. and Zanetti G. (2008) Structural and functional diversity of ferredoxin-NADP+ reductases. *Archives of Biochemistry and Biophysics* **474**, 283–291.

Amenabar M. J., Shock E. L., Roden E. E., Peters J. W. and Boyd E. S. (2017) Microbial substrate preference dictated by energy demand rather than supply. *Nature geoscience* **10**, 577–581.

Bayer B., Pelikan C., Bittner M. J., Reinthaler T., Könneke M., Herndl G. J. and Offre P. (2019) Proteomic response of three marine ammonia-oxidizing archaea to hydrogen peroxide and their metabolic interactions with a heterotrophic alphaproteobacterium. *Msystems* **4**, e00181-19.

Bender A. L. D., Suess M., Chitwood D. H. and Bradley A. S. (2016) Investigating genetic loci that encode plant-derived paleoclimate proxies. In pp. PP24B-03.

Boyd E. S., Hamilton T. L., Wang J., He L. and Zhang C. L. (2013) The Role of Tetraether Lipid Composition in the Adaptation of Thermophilic Archaea to Acidity. *Front. Microbiol.* **4**.

Boyd E. S., Pearson A., Pi Y., Li W.-J., Zhang Y. G., He L., Zhang C. L. and Geesey G. G. (2011) Temperature and pH controls on glycerol dibiphytanyl glycerol tetraether lipid composition in the hyperthermophilic crenarchaeon Acidilobus sulfurireducens. *Extremophiles* **15**, 59–65.

Bräsen C., Esser D., Rauch B. and Siebers B. (2014) Carbohydrate metabolism in Archaea: current insights into unusual enzymes and pathways and their regulation. *Microbiology and Molecular Biology Reviews* **78**, 89–175.

Buckel W. and Thauer R. K. (2013) Energy conservation via electron bifurcating ferredoxin reduction and proton/Na+ translocating ferredoxin oxidation. *Biochimica et Biophysica Acta (BBA)-Bioenergetics* **1827**, 94–113.

Buckel W. and Thauer R. K. (2018) Flavin-based electron bifurcation, ferredoxin, flavodoxin, and anaerobic respiration with protons (Ech) or NAD+ (Rnf) as electron acceptors: A historical review. *Frontiers in microbiology* **9**, 401.

Campbell B. J., Li C., Sessions A. L. and Valentine D. L. (2009) Hydrogen isotopic fractionation in lipid biosynthesis by H2-consuming Desulfobacterium autotrophicum. *Geochimica et Cosmochimica Acta* **73**, 2744–2757.

Campbell B. J., Sessions A. L., Fox D. N., Paul B. G., Qin Q., Kellermann M. Y. and Valentine D. L. (2017) Minimal influence of [NiFe] hydrogenase on hydrogen isotope fractionation in H2-oxidizing cupriavidus necator. *Frontiers in microbiology* **8**, 1886.

Chen A., Dale Poulter C. and Kroon P. A. (1994) Isoprenyl diphosphate synthases: protein sequence comparisons, a phylogenetic tree, and predictions of secondary structure. *Protein Science* **3**, 600–607.

Chen A. and Poulter C. (1993) Purification and characterization of farnesyl diphosphate/geranylgeranyl diphosphate synthase. A thermostable bifunctional enzyme from Methanobacterium thermoautotrophicum. *Journal of Biological Chemistry* **268**, 11002–11007.

1022 Cobban A., Zhang Y., Zhou A., Weber Y., Elling F. J., Pearson A. and Leavitt W. D. (2020)
1023 Multiple environmental parameters impact lipid cyclization in Sulfolobus acidocaldarius.
1024 *Environmental Microbiology* **22**, 4046–4056.
1025 Dawson K. S., Osburn M. R., Sessions A. L. and Orphan V. J. (2015) Metabolic associations
1026 with archaea drive shifts in hydrogen isotope fractionation in sulfate-reducing bacterial
1027 lipids in cocultures and methane seeps. *Geobiology* **13**, 462–477.
1028 Dirghangi S. S. and Pagani M. (2013) Hydrogen isotope fractionation during lipid biosynthesis
1029 by Haloarcula marismortui. *Geochimica et Cosmochimica Acta* **119**, 381–390.
1030 Dunkley Jones T., Eley Y. L., Thomson W., Greene S. E., Mandel I., Edgar K. and Bendle J. A.
1031 (2020) OPTiMAL: a new machine learning approach for GDGT-based
1032 palaeothermometry. *Climate of the Past* **16**, 2599–2617.
1033 Elling F. J., Gottschalk J., Doeana K. D., Kusch S., Hurley S. J. and Pearson A. (2019) Archaeal
1034 lipid biomarker constraints on the Paleocene-Eocene carbon isotope excursion. *Nature*
1035 *communications* **10**, 1–10.
1036 Elling F. J., Könneke M., Nicol G. W., Stieglmeier M., Bayer B., Spieck E., de la Torre J. R.,
1037 Becker K. W., Thomm M. and Prosser J. I. (2017) Chemotaxonomic characterisation of
1038 the thaumarchaeal lipidome. *Environmental microbiology* **19**, 2681–2700.
1039 Estep M. F. and Hoering T. C. (1980) Biogeochemistry of the stable hydrogen isotopes.
1040 *Geochimica et Cosmochimica Acta* **44**, 1197–1206.
1041 Feyhl-Buska J., Chen Y., Jia C., Wang J.-X., Zhang C. L. and Boyd E. S. (2016) Influence of
1042 growth phase, pH, and temperature on the abundance and composition of tetraether lipids
1043 in the Thermoacidophile Picrophilus torridus. *Frontiers in microbiology* **7**, 1323.
1044 Fuhrer T. and Sauer U. (2009) Different biochemical mechanisms ensure network-wide
1045 balancing of reducing equivalents in microbial metabolism. *Journal of bacteriology* **191**,
1046 2112–2121.
1047 Gao L., Hou J., Toney J., MacDonald D. and Huang Y. (2011) Mathematical modeling of the
1048 aquatic macrophyte inputs of mid-chain n-alkyl lipids to lake sediments: Implications for
1049 interpreting compound specific hydrogen isotopic records. *Geochimica et Cosmochimica*
1050 *Acta* **75**, 3781–3791.
1051 Gao L., Zheng M., Fraser M. and Huang Y. (2014) Comparable hydrogen isotopic fractionation
1052 of plant leaf wax n-alkanoic acids in arid and humid subtropical ecosystems.
1053 *Geochemistry, Geophysics, Geosystems* **15**, 361–373.
1054 Gat J. R. (1996) Oxygen and hydrogen isotopes in the hydrologic cycle. *Annual Review of Earth*
1055 *and Planetary Sciences* **24**, 225–262.
1056 Hayakawa H., Motoyama K., Sobue F., Ito T., Kawaide H., Yoshimura T. and Hemmi H. (2018)
1057 Modified mevalonate pathway of the archaeon Aeropyrum pernix proceeds via trans-
1058 anhydromevalonate 5-phosphate. *Proceedings of the National Academy of Sciences* **115**,
1059 10034–10039.
1060 Hayes J. (2001) Fractionation of the isotopes of carbon and hydrogen in biosynthetic processes,
1061 pp. 225Ð277. *Stable isotope geochemistry* **43**.
1062 Heinzelmann S. M., Chivall D., M'Boule D., Sinke-Schoen D., Villanueva L., Damsté J. S. S.,
1063 Schouten S., Van der Meer M. T. and Oren A. (2015a) Comparison of the effect of
1064 salinity on the D/H ratio of fatty acids of heterotrophic and photoautotrophic
1065 microorganisms. *FEMS microbiology letters* **362**.
1066 Heinzelmann S. M., Villanueva L., Lipsewers Y. A., Sinke-Schoen D., Damste J. S. S., Schouten
1067 S. and van der Meer M. T. (2018) Assessing the metabolism of sedimentary microbial

communities using the hydrogen isotopic composition of fatty acids. *Organic Geochemistry* **124**, 123–132.

Heinzelmann S. M., Villanueva L., Sinke-Schoen D., Sinninghe Damsté J. S., Schouten S. and Van der Meer M. T. (2015b) Impact of metabolism and growth phase on the hydrogen isotopic composition of microbial fatty acids. *Frontiers in microbiology* **6**, 408.

Hoffmann-Sell L., Birgel D., Arning E. T., Föllmi K. B. and Peckmann J. (2011) Archaeal lipids in Neogene dolomites (Monterey and Sisquoc Formations, California)–Planktic versus benthic archaeal sources. *Organic geochemistry* **42**, 593–604.

Hou J., D'Andrea W. J. and Huang Y. (2008) Can sedimentary leaf waxes record D/H ratios of continental precipitation? Field, model, and experimental assessments. *Geochimica et Cosmochimica Acta* **72**, 3503–3517.

Hurley S. J., Elling F. J., Könneke M., Buchwald C., Wankel S. D., Santoro A. E., Lipp J. S., Hinrichs K.-U. and Pearson A. (2016) Influence of ammonia oxidation rate on thaumarchaeal lipid composition and the TEX86 temperature proxy. *Proceedings of the National Academy of Sciences* **113**, 7762–7767.

Isobe K., Ogawa T., Hirose K., Yokoi T., Yoshimura T. and Hemmi H. (2014) Geranylgeranyl Reductase and Ferredoxin from Methanosarcina acetivorans Are Required for the Synthesis of Fully Reduced Archaeal Membrane Lipid in Escherichia coli Cells. *Journal of Bacteriology* **196**, 417–423.

Jackson J. B., Peake S. J. and White S. A. (1999) Structure and mechanism of proton-translocating transhydrogenase. *FEBS letters* **464**, 1–8.

Jain S., Caforio A. and Driessen A. J. (2014) Biosynthesis of archaeal membrane ether lipids. *Frontiers in microbiology* **5**, 641.

Kahmen A., Dawson T. E., Vieth A. and Sachse D. (2011) Leaf wax n-alkane δD values are determined early in the ontogeny of Populus trichocarpa leaves when grown under controlled environmental conditions. *Plant, Cell & Environment* **34**, 1639–1651.

Kaneko M., Kitajima F. and Naraoka H. (2011) Stable hydrogen isotope measurement of archaeal ether-bound hydrocarbons. *Organic Geochemistry* **42**, 166–172.

Keller Y., Bouvier F., d'Harlingue A. and Camara B. (1998) Metabolic compartmentation of plastid prenyllipid biosynthesis: evidence for the involvement of a multifunctional geranylgeranyl reductase. *European Journal of Biochemistry* **251**, 413–417.

Kellermann M. Y., Yoshinaga M. Y., Wegener G., Krukenberg V. and Hinrichs K.-U. (2016) Tracing the production and fate of individual archaeal intact polar lipids using stable isotope probing. *Organic Geochemistry* **95**, 13–20.

Kim J.-G., Park S.-J., Damsté J. S. S., Schouten S., Rijpstra W. I. C., Jung M.-Y., Kim S.-J., Gwak J.-H., Hong H. and Si O.-J. (2016) Hydrogen peroxide detoxification is a key mechanism for growth of ammonia-oxidizing archaea. *Proceedings of the National Academy of Sciences* **113**, 7888–7893.

Kim J.-H., Schouten S., Hopmans E. C., Donner B. and Damsté J. S. S. (2008) Global sediment core-top calibration of the TEX86 paleothermometer in the ocean. *Geochimica et Cosmochimica Acta* **72**, 1154–1173.

Kim J.-H., Van der Meer J., Schouten S., Helmke P., Willmott V., Sangiorgi F., Koç N., Hopmans E. C. and Damsté J. S. S. (2010) New indices and calibrations derived from the distribution of crenarchaeal isoprenoid tetraether lipids: Implications for past sea surface temperature reconstructions. *Geochimica et Cosmochimica Acta* **74**, 4639–4654.

1113 Koga Y. and Morii H. (2007) Biosynthesis of ether-type polar lipids in archaea and evolutionary
1114 considerations. *Microbiology and Molecular Biology Reviews* **71**, 97–120.
1115 Könneke M., Bernhard A. E., José R., Walker C. B., Waterbury J. B. and Stahl D. A. (2005)
1116 Isolation of an autotrophic ammonia-oxidizing marine archaeon. *Nature* **437**, 543–546.
1117 Könneke M., Schubert D. M., Brown P. C., Hügler M., Standfest S., Schwander T., von
1118 Borzyskowski L. S., Erb T. J., Stahl D. A. and Berg I. A. (2014) Ammonia-oxidizing
1119 archaea use the most energy-efficient aerobic pathway for CO2 fixation. *Proceedings of*
1120 *the National Academy of Sciences* **111**, 8239–8244.
1121 Kopf S., Davidheiser-Kroll B. and Kocken I. (2021) Isoreader: An R package to read stable
1122 isotope data files for reproducible research. *Journal of Open Source Software* **6**, 2878.
1123 Kopf S. H. (2015) From lakes to lungs: Assessing microbial activity in diverse environments.
1124 Kopf S. H., McGlynn S. E., Green-Saxena A., Guan Y., Newman D. K. and Orphan V. J. (2015)
1125 Heavy water and 15 N labelling with N ano SIMS analysis reveals growth rate-dependent
1126 metabolic heterogeneity in chemostats. *Environmental microbiology* **17**, 2542–2556.
1127 Kreuzer-Martin H. W., Lott M. J., Ehleringer J. R. and Hegg E. L. (2006) Metabolic processes
1128 account for the majority of the intracellular water in log-phase Escherichia coli cells as
1129 revealed by hydrogen isotopes. *Biochemistry* **45**, 13622–13630.
1130 Lattaud J., De Jonge C., Pearson A., Elling F. J. and Eglinton T. I. (2021) Microbial lipid
1131 signatures in Arctic deltaic sediments–Insights into methane cycling and climate
1132 variability. *Organic Geochemistry* **157**, 104242.
1133 Leavitt William D., Flynn T. M., Suess M. K. and Bradley A. S. (2016) Transhydrogenase and
1134 Growth Substrate Influence Lipid Hydrogen Isotope Ratios in Desulfovibrio alaskensis
1135 G20. *Frontiers in Microbiology* **07**.
1136 Leavitt W. D., Murphy S. J.-L., Lynd L. R. and Bradley A. S. (2017) Hydrogen isotope
1137 composition of Thermoanaerobacterium saccharolyticum lipids: Comparing wild type
1138 with a nfn- transhydrogenase mutant. *Organic Geochemistry* **113**, 239–241.
1139 Leavitt William D, Venceslau S. S., Pereira I. A., Johnston D. T. and Bradley A. S. (2016)
1140 Fractionation of sulfur and hydrogen isotopes in Desulfovibrio vulgaris with perturbed
1141 DsrC expression. *FEMS microbiology letters* **363**.
1142 Leavitt W. D., Venceslau S. S., Waldbauer J., Smith D. A., Pereira I. A. C. and Bradley A. S.
1143 (2019) Proteomic and isotopic response of Desulfovibrio vulgaris to DsrC perturbation.
1144 *Frontiers in microbiology* **10**, 658.
1145 Lengger S. K., Weber Y., Taylor K. W., Kopf S. H., Berstan R., Bull I. D., Mayser J., Leavitt W.
1146 D., Blewett J. and Pearson A. (2021) Determination of the δ2H values of high molecular
1147 weight lipids by high-temperature gas chromatography coupled to isotope ratio mass
1148 spectrometry. *Rapid Communications in Mass Spectrometry* **35**, e8983.
1149 Liu H., Cao Y., Hu J., Liu Z. and Liu W. (2022) Substantial peak size effect on compound-
1150 specific δD values analyzed on isotope ratio mass spectrometry. *Chemical Geology*,
1151 120721.
1152 Luo Y.-H., Steinberg L., Suda S., Kumazawa S. and Mitsui A. (1991) Extremely low D/H ratios
1153 of photoproduced hydrogen by cyanobacteria. *Plant and cell physiology* **32**, 897–900.
1154 Maloney A. E., Shinneman A. L., Hemeon K. and Sachs J. P. (2016) Exploring lipid 2H/1H
1155 fractionation mechanisms in response to salinity with continuous cultures of the diatom
1156 Thalassiosira pseudonana. *Organic Geochemistry* **101**, 154–165.

Martens-Habbena W., Berube P. M., Urakawa H., José R. and Stahl D. A. (2009) Ammonia oxidation kinetics determine niche separation of nitrifying Archaea and Bacteria. *Nature* **461**, 976–979.

McFarlin J. M., Axford Y., Masterson A. L. and Osburn M. R. (2019) Calibration of modern sedimentary δ2H plant wax-water relationships in Greenland lakes. *Quaternary Science Reviews* **225**, 105978.

McInerney F. A., Helliker B. R. and Freeman K. H. (2011) Hydrogen isotope ratios of leaf wax n-alkanes in grasses are insensitive to transpiration. *Geochimica et Cosmochimica Acta* **75**, 541–554.

van der Meer M. T., Benthien A., French K. L., Epping E., Zondervan I., Reichart G.-J., Bijma J., Damsté J. S. S. and Schouten S. (2015) Large effect of irradiance on hydrogen isotope fractionation of alkenones in Emiliania huxleyi. *Geochimica et Cosmochimica Acta* **160**, 16–24.

Murakami M., Shibuya K., Nakayama T., Nishino T., Yoshimura T. and Hemmi H. (2007) Geranylgeranyl reductase involved in the biosynthesis of archaeal membrane lipids in the hyperthermophilic archaeon Archaeoglobus fulgidus. *The FEBS journal* **274**, 805–814.

Nishimura Y. and Eguchi T. (2006) Biosynthesis of archaeal membrane lipids: digeranylgeranylglycerophospholipid reductase of the thermoacidophilic archaeon Thermoplasma acidophilum. *Journal of biochemistry* **139**, 1073–1081.

Nunn C. E., Johnsen U., Schönheit P., Fuhrer T., Sauer U., Hough D. W. and Danson M. J. (2010) Metabolism of pentose sugars in the hyperthermophilic archaea Sulfolobus solfataricus and Sulfolobus acidocaldarius. *Journal of Biological Chemistry* **285**, 33701–33709.

Oger P. M. and Cario A. (2013) Adaptation of the membrane in Archaea. *Biophysical chemistry* **183**, 42–56.

Osburn M. R., Dawson K. S., Fogel M. L. and Sessions A. L. (2016) Fractionation of hydrogen isotopes by sulfate-and nitrate-reducing bacteria. *Frontiers in microbiology* **7**, 1166.

Pearson A. (2019) Resolving a piece of the archaeal lipid puzzle. *Proceedings of the National Academy of Sciences* **116**, 22423–22425.

Pearson A., Hurley S. J., Walter S. R. S., Kusch S., Lichtin S. and Zhang Y. G. (2016) Stable carbon isotope ratios of intact GDGTs indicate heterogeneous sources to marine sediments. *Geochimica et Cosmochimica Acta* **181**, 18–35.

Pearson A. and Ingalls A. E. (2013) Assessing the use of archaeal lipids as marine environmental proxies. *Annual Review of Earth and Planetary Sciences* **41**, 359–384.

Peregrina J. R., Sánchez-Azqueta A., Herguedas B., Martínez-Júlvez M. and Medina M. (2010) Role of specific residues in coenzyme binding, charge–transfer complex formation, and catalysis in Anabaena ferredoxin NADP+-reductase. *Biochimica et Biophysica Acta (BBA) - Bioenergetics* **1797**, 1638–1646.

Polik C. A., Elling F. J. and Pearson A. (2018) Impacts of paleoecology on the TEX86 sea surface temperature proxy in the Pliocene-Pleistocene Mediterranean Sea. *Paleoceanography and Paleoclimatology* **33**, 1472–1489.

Poudel S., Dunham E. C., Lindsay M. R., Amenabar M. J., Fones E. M., Colman D. R. and Boyd E. S. (2018) Origin and evolution of flavin-based electron bifurcating enzymes. *Frontiers in microbiology* **9**, 1762.

1201 Powers L., Werne J. P., Vanderwoude A. J., Damsté J. S. S., Hopmans E. C. and Schouten S.
1202 (2010) Applicability and calibration of the TEX86 paleothermometer in lakes. *Organic*
1203 *Geochemistry* **41**, 404–413.
1204 Qin W., Amin S. A., Lundeen R. A., Heal K. R., Martens-Habbena W., Turkarslan S., Urakawa
1205 H., Costa K. C., Hendrickson E. L. and Wang T. (2018) Stress response of a marine
1206 ammonia-oxidizing archaeon informs physiological status of environmental populations.
1207 *The ISME journal* **12**, 508–519.
1208 Qin W., Amin S. A., Martens-Habbena W., Walker C. B., Urakawa H., Devol A. H., Ingalls A.
1209 E., Moffett J. W., Armbrust E. V. and Stahl D. A. (2014) Marine ammonia-oxidizing
1210 archaeal isolates display obligate mixotrophy and wide ecotypic variation. *Proceedings of*
1211 *the National Academy of Sciences* **111**, 12504–12509.
1212 Quehenberger J., Pittenauer E., Allmaier G. and Spadiut O. (2020) The influence of the specific
1213 growth rate on the lipid composition of Sulfolobus acidocaldarius. *Extremophiles* **24**,
1214 413.
1215 Ren M., Feng X., Huang Y., Wang H., Hu Z., Clingenpeel S., Swan B. K., Fonseca M. M.,
1216 Posada D., Stepanauskas R., Hollibaugh J. T., Foster P. G., Woyke T. and Luo H. (2019)
1217 Phylogenomics suggests oxygen availability as a driving force in Thaumarchaeota
1218 evolution. *The ISME Journal* **13**, 2150–2161.
1219 Robert F. (2001) The Origin of Water on Earth. *Science* **293**, 1056.
1220 Sachs J. P. (2014) Hydrogen Isotope Signatures in the Lipids of Phytoplankton. In *Treatise on*
1221 *Geochemistry* Elsevier. pp. 79–94.
1222 Sachs J. P. and Kawka O. E. (2015) The influence of growth rate on 2H/1H fractionation in
1223 continuous cultures of the coccolithophorid Emiliania huxleyi and the diatom
1224 Thalassiosira pseudonana. *Plos one* **10**, e0141643.
1225 Sachs J. P., Maloney A. E. and Gregersen J. (2017) Effect of light on 2H/1H fractionation in
1226 lipids from continuous cultures of the diatom Thalassiosira pseudonana. *Geochimica et*
1227 *Cosmochimica Acta* **209**, 204–215.
1228 Sachs J. P., Maloney A. E., Gregersen J. and Paschall C. (2016) Effect of salinity on 2H/1H
1229 fractionation in lipids from continuous cultures of the coccolithophorid Emiliania
1230 huxleyi. *Geochimica et Cosmochimica Acta* **189**, 96–109.
1231 Sachse D., Billault I., Bowen G. J., Chikaraishi Y., Dawson T. E., Feakins S. J., Freeman K. H.,
1232 Magill C. R., McInerney F. A. and Van Der Meer M. T. (2012) Molecular
1233 paleohydrology: interpreting the hydrogen-isotopic composition of lipid biomarkers from
1234 photosynthesizing organisms. *Annual Review of Earth and Planetary Sciences* **40**, 221–
1235 249.
1236 Sachse D., Gleixner G., Wilkes H. and Kahmen A. (2010) Leaf wax n-alkane δD values of field-
1237 grown barley reflect leaf water δD values at the time of leaf formation. *Geochimica et*
1238 *Cosmochimica Acta* **74**, 6741–6750.
1239 Sánchez-Azqueta A., Herguedas B., Hurtado-Guerrero R., Hervás M., Navarro J. A., Martínez-
1240 Júlvez M. and Medina M. (2014) A hydrogen bond network in the active site of
1241 Anabaena ferredoxin-NADP+ reductase modulates its catalytic efficiency. *Biochimica et*
1242 *Biophysica Acta (BBA) - Bioenergetics* **1837**, 251–263.
1243 Santoro A. E. and Casciotti K. L. (2011) Enrichment and characterization of ammonia-oxidizing
1244 archaea from the open ocean: phylogeny, physiology and stable isotope fractionation. *The*
1245 *ISME journal* **5**, 1796–1808.

1246 Sasaki D., Fujihashi M., Iwata Y., Murakami M., Yoshimura T., Hemmi H. and Miki K. (2011)
1247 Structure and Mutation Analysis of Archaeal Geranylgeranyl Reductase. *Journal of*
1248 *Molecular Biology* **409**, 543–557.
1249 Sato S., Murakami M., Yoshimura T. and Hemmi H. (2008) Specific Partial Reduction of
1250 Geranylgeranyl Diphosphate by an Enzyme from the Thermoacidophilic Archaeon
1251 *Sulfolobus acidocaldarius* Yields a Reactive Prenyl Donor, Not a Dead-End Product. *J*
1252 *Bacteriol* **190**, 3923–3929.
1253 Sauer U., Canonaco F., Heri S., Perrenoud A. and Fischer E. (2004) The soluble and membrane-
1254 bound transhydrogenases UdhA and PntAB have divergent functions in NADPH
1255 metabolism of Escherichia coli. *Journal of Biological Chemistry* **279**, 6613–6619.
1256 Schimmelmann A., Sessions A. L. and Mastalerz M. (2006) Hydrogen isotopic (D/H)
1257 composition of organic matter during diagenesis and thermal maturation. *Annu. Rev.*
1258 *Earth Planet. Sci.* **34**, 501–533.
1259 Schouten S., Hopmans E. C. and Damsté J. S. S. (2013) The organic geochemistry of glycerol
1260 dialkyl glycerol tetraether lipids: A review. *Organic geochemistry* **54**, 19–61.
1261 Schouten S., Hopmans E. C., Schefuß E. and Damste J. S. S. (2002) Distributional variations in
1262 marine crenarchaeotal membrane lipids: a new tool for reconstructing ancient sea water
1263 temperatures? *Earth and Planetary Science Letters* **204**, 265–274.
1264 Schouten S., Ossebaar J., Schreiber K., Kienhuis M., Langer G., Benthien A. and Bijma J. (2006)
1265 The effect of temperature, salinity and growth rate on the stable hydrogen isotopic
1266 composition of long chain alkenones produced by Emiliania huxleyi and Gephyrocapsa
1267 oceanica. *Biogeosciences* **3**, 113–119.
1268 Sessions A. L. (2016) Factors controlling the deuterium contents of sedimentary hydrocarbons.
1269 *Organic Geochemistry* **96**, 43–64.
1270 Sessions A. L., Burgoyne T. W., Schimmelmann A. and Hayes J. M. (1999) Fractionation of
1271 hydrogen isotopes in lipid biosynthesis. *Organic Geochemistry* **30**, 1193–1200.
1272 Sessions A. L., Jahnke L. L., Schimmelmann A. and Hayes J. M. (2002) Hydrogen isotope
1273 fractionation in lipids of the methane-oxidizing bacterium Methylococcus capsulatus.
1274 *Geochimica et Cosmochimica Acta* **66**, 3955–3969.
1275 Sessions A. L., Sylva S. P., Summons R. E. and Hayes J. M. (2004) Isotopic exchange of carbon-
1276 bound hydrogen over geologic timescales. *Geochimica et Cosmochimica Acta* **68**, 1545–
1277 1559.
1278 Shafiee R. T., Snow J. T., Hester S., Zhang Q. and Rickaby R. E. (2022) Proteomic response of
1279 the marine ammonia-oxidising archaeon Nitrosopumilus maritimus to iron limitation
1280 reveals strategies to compensate for nutrient scarcity. *Environmental Microbiology* **24**,
1281 835–849.
1282 Shah S. R., Mollenhauer G., Ohkouchi N., Eglinton T. I. and Pearson A. (2008) Origins of
1283 archaeal tetraether lipids in sediments: Insights from radiocarbon analysis. *Geochimica et*
1284 *Cosmochimica Acta* **72**, 4577–4594.
1285 Sinninghe Damsté J., Pancost R. and Hopmans E. (2001) Archaeal lipids in Mediterranean Cold
1286 Seeps: Molecular proxies for anaerobic methane oxidation. *Geochimica et Cosmochimica*
1287 *Acta* **65**, 1611.
1288 Sinninghe Damsté J. S., Weber Y., Zopfi J., Lehmann M. F. and Niemann H. (2022)
1289 Distributions and sources of isoprenoidal GDGTs in Lake Lugano and other central
1290 European (peri-)alpine lakes: Lessons for their use as paleotemperature proxies.
1291 *Quaternary Science Reviews* **277**, 107352.

1292 Smith F. A. and Freeman K. H. (2006) Influence of physiology and climate on δD of leaf wax n-
1293 alkanes from C3 and C4 grasses. *Geochimica et Cosmochimica Acta* **70**, 1172–1187.
1294 Spaans S. K., Weusthuis R. A., Van Der Oost J. and Kengen S. W. (2015) NADPH-generating
1295 systems in bacteria and archaea. *Frontiers in microbiology* **6**, 742.
1296 Taenzer L., Labidi J., Masterson A. L., Feng X., Rumble III D., Young E. D. and Leavitt W. D.
1297 (2020) Low Δ12CH2D2 values in microbialgenic methane result from combinatorial
1298 isotope effects. *Geochimica et Cosmochimica Acta* **285**, 225–236.
1299 Taylor K. W., Huber M., Hollis C. J., Hernandez-Sanchez M. T. and Pancost R. D. (2013) Re-
1300 evaluating modern and Palaeogene GDGT distributions: Implications for SST
1301 reconstructions. *Global and Planetary Change* **108**, 158–174.
1302 Tierney J. E. and Tingley M. P. (2014) A Bayesian, spatially-varying calibration model for the
1303 TEX86 proxy. *Geochimica et Cosmochimica Acta* **127**, 83–106.
1304 Tierney J. E. and Tingley M. P. (2015) A TEX 86 surface sediment database and extended
1305 Bayesian calibration. *Scientific data* **2**, 1–10.
1306 Tipple B. J., Berke M. A., Doman C. E., Khachaturyan S. and Ehleringer J. R. (2013) Leaf-wax
1307 n-alkanes record the plant–water environment at leaf flush. *Proceedings of the National*
1308 *Academy of Sciences* **110**, 2659–2664.
1309 Tourte M., Schaeffer P., Grossi V. and Oger P. M. (2022) Membrane adaptation in the
1310 hyperthermophilic archaeon Pyrococcus furiosus relies upon a novel strategy involving
1311 glycerol monoalkyl glycerol tetraether lipids. *Environmental Microbiology* **24**, 2029–
1312 2046.
1313 Valentine D. L. (2007) Adaptations to energy stress dictate the ecology and evolution of the
1314 Archaea. *Nature Reviews Microbiology* **5**, 316–323.
1315 Valentine D., Sessions A., Tyler S. and Chidthaisong A. (2004) Hydrogen isotope fractionation
1316 during H2/CO2 acetogenesis: hydrogen utilization efficiency and the origin of lipid-
1317 bound hydrogen. *Geobiology* **2**, 179–188.
1318 Wakeham S. G., Lewis C. M., Hopmans E. C., Schouten S. and Damsté J. S. S. (2003) Archaea
1319 mediate anaerobic oxidation of methane in deep euxinic waters of the Black Sea.
1320 *Geochimica et Cosmochimica Acta* **67**, 1359–1374.
1321 Walker C. B., De La Torre J., Klotz M., Urakawa H., Pinel N., Arp D., Brochier-Armanet C.,
1322 Chain P., Chan P. and Gollabgir A. (2010) Nitrosopumilus maritimus genome reveals
1323 unique mechanisms for nitrification and autotrophy in globally distributed marine
1324 crenarchaea. *Proceedings of the National Academy of Sciences* **107**, 8818–8823.
1325 Wang Y., Sessions A. L., Nielsen R. J. and Goddard III W. A. (2009) Equilibrium 2H/1H
1326 fractionations in organic molecules: I. Experimental calibration of ab initio calculations.
1327 *Geochimica et Cosmochimica Acta* **73**, 7060–7075.
1328 Wegener G., Kellermann M. Y. and Elvert M. (2016) Tracking activity and function of
1329 microorganisms by stable isotope probing of membrane lipids. *Current Opinion in*
1330 *Biotechnology* **41**, 43–52.
1331 Weijers J. W., Schouten S., Schefuß E., Schneider R. R. and Damste J. S. S. (2009)
1332 Disentangling marine, soil and plant organic carbon contributions to continental margin
1333 sediments: a multi-proxy approach in a 20,000 year sediment record from the Congo
1334 deep-sea fan. *Geochimica et Cosmochimica Acta* **73**, 119–132.
1335 Wijker R. S., Sessions A. L., Fuhrer T. and Phan M. (2019) 2H/1H variation in microbial lipids
1336 is controlled by NADPH metabolism. *Proceedings of the National Academy of Sciences*
1337 **116**, 12173–12182.

Wolfshorndl M., Danford R. and Sachs J. P. (2019) 2H/1H fractionation in microalgal lipids from the North Pacific Ocean: Growth rate and irradiance effects. *Geochimica et Cosmochimica Acta* **246**, 317–338.

Wu W., Meador T. B., Könneke M., Elvert M., Wegener G. and Hinrichs K. (2020) Substrate-dependent incorporation of carbon and hydrogen for lipid biosynthesis by Methanosarcina barkeri. *Environmental Microbiology Reports* **12**, 555–567.

Zeng Z., Chen H., Yang H., Chen Y., Yang W., Feng X., Pei H. and Welander P. V. (2022) Identification of a protein responsible for the synthesis of archaeal membrane-spanning GDGT lipids. *Nature Communications* **13**, 1545.

Zeng Z., Liu X.-L., Farley K. R., Wei J. H., Metcalf W. W., Summons R. E. and Welander P. V. (2019) GDGT cyclization proteins identify the dominant archaeal sources of tetraether lipids in the ocean. *Proc Natl Acad Sci USA*, 201909306.

Zhang X., Gillespie A. L. and Sessions A. L. (2009) Large D/H variations in bacterial lipids reflect central metabolic pathways. *Proceedings of the National Academy of Sciences* **106**, 12580–12586.

Zhang Y. G., Pagani M. and Wang Z. (2016) Ring Index: A new strategy to evaluate the integrity of TEX86 paleothermometry. *Paleoceanography* **31**, 220–232.

Zhang Y. G., Zhang C. L., Liu X.-L., Li L., Hinrichs K.-U. and Noakes J. E. (2011) Methane Index: A tetraether archaeal lipid biomarker indicator for detecting the instability of marine gas hydrates. *Earth and Planetary Science Letters* **307**, 525–534.

Zhou A., Weber Y., Chiu B. K., Elling F. J., Cobban A. B., Pearson A. and Leavitt W. D. (2020) Energy flux controls tetraether lipid cyclization in Sulfolobus acidocaldarius. *Environmental microbiology* **22**, 343–353.

Figure 1:

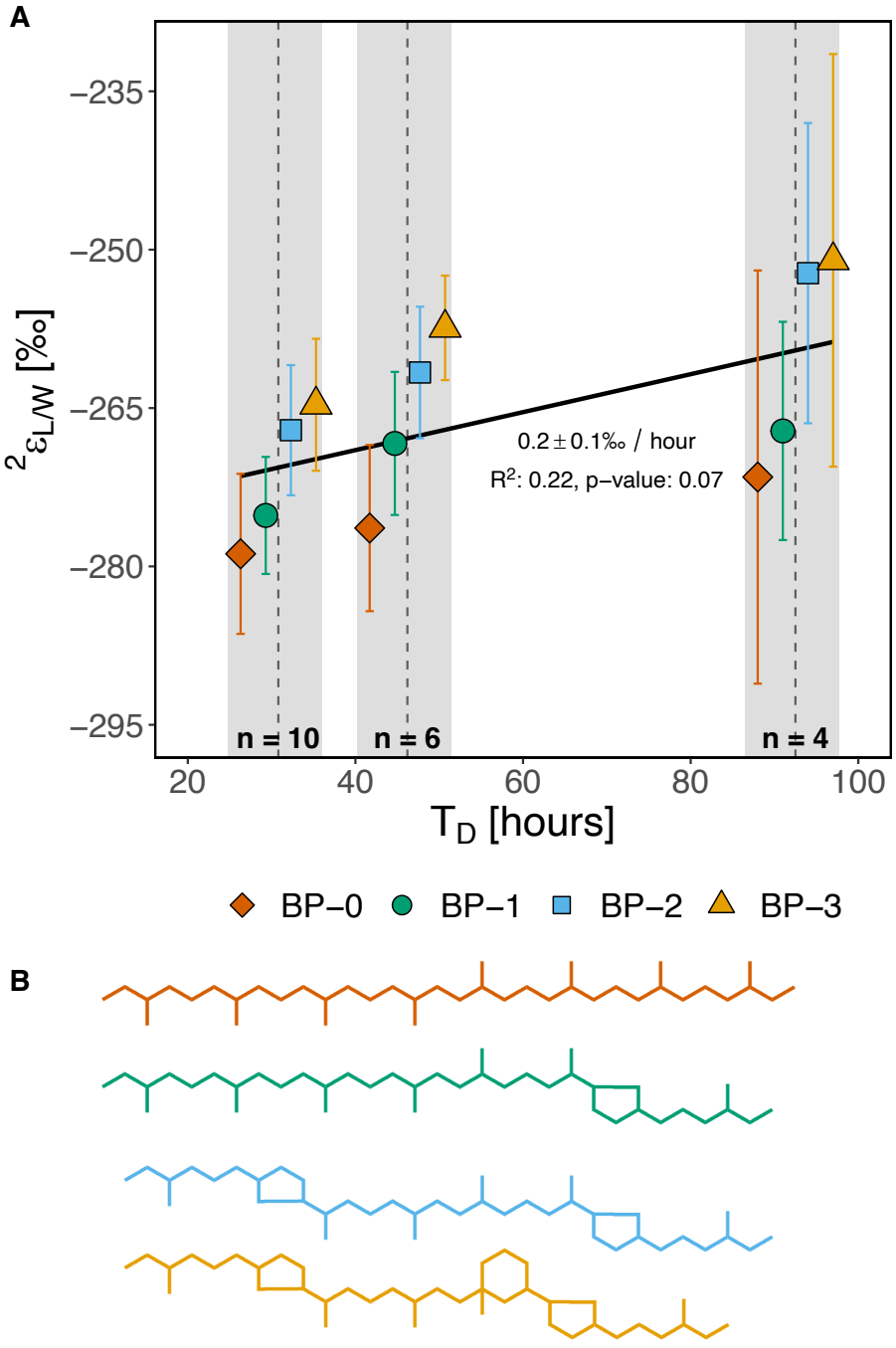

Figure 1. (**A**) The hydrogen isotope fractionation ($^2\varepsilon_{L/W}$) between growth medium water and biphytanes (BPs) in response to doubling time (T_D) for *N. maritimus* cultivated at 28 °C and pH 7.5-7.6. Black line shows the slope (‰ / hour) for abundance-weighted linear regression of all biphytane $^2\varepsilon_{L/W}$ values vs. T_D. (**B**) Structures of the BPs (color-coded to match data shown in A).

Figure 2:

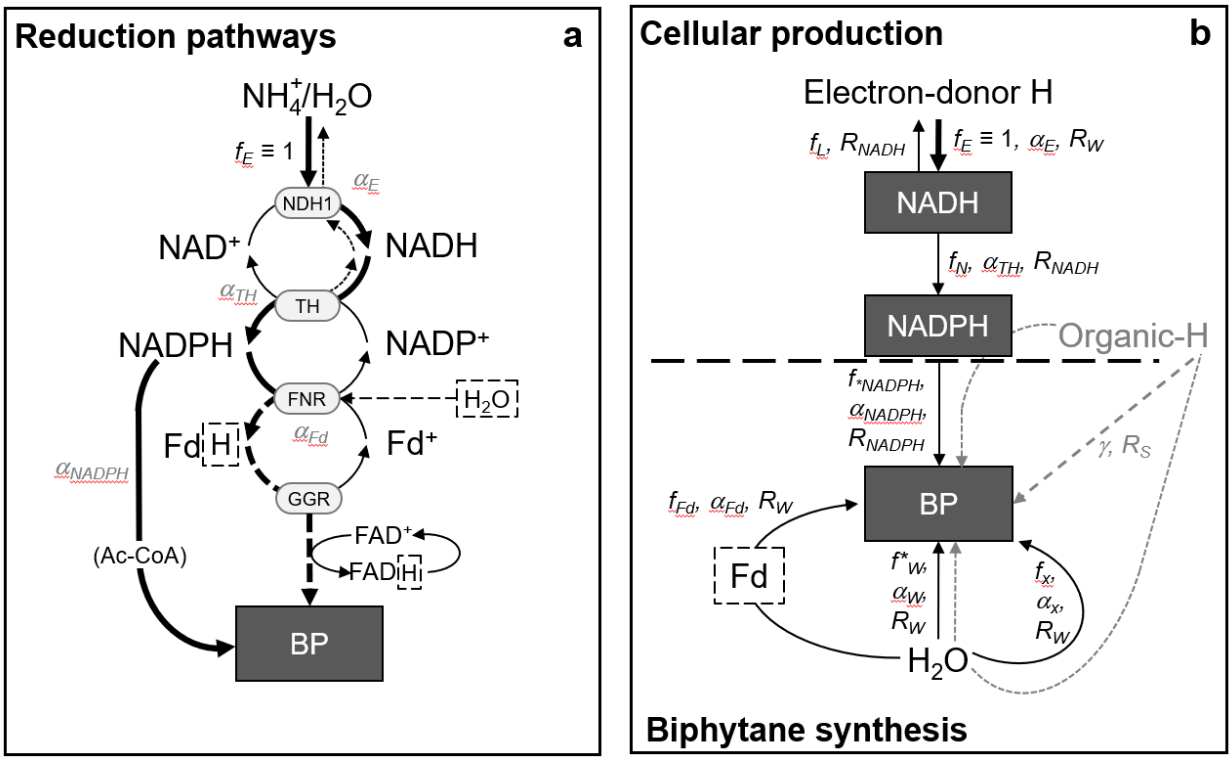

Figure 2. (a) Sources of biosynthetic H for biphytane (BP) synthesis in *N. maritimus*. Respiratory complex 1 (NDH1) and an unknown transhydrogenase (TH) transfer H to NADPH. This NADPH either is a direct source of anabolic H to BPs (via Ac-CoA and further reactions; see Figure 3) or the e^- are transferred to ferredoxin-NAD^+ reductase (FNR, which takes H^+ from H_2O). FNR is the suggested donor for geranylgeranyl reductase (GGR), which uses FADH as a cofactor. See main text for further details. (b) The resulting isotope flux balance model with simplified sources of H. Cellular production sums above the horizontal dashed line, whereas biphytane sums below. f_i = fractional fluxes; $a_i = {}^2H/{}^1H$ kinetic isotope effects; $R_i = {}^2H/{}^1H$ isotope ratios; concept according to Wijker et al., 2019. The Cellular production module controls the isotope balance of NADPH, which flows into the Biphytane synthesis module. Thus, f_N and f_{*NADPH} are not equal; f_N is a fraction of total available reducing power, f_E (with the remainder leaked via the NADH pool, f_L), while f_{*NADPH} is a fraction of biphytane stoichiometric flux. Processes that would incorporate H from acetate and organic substrates are shown in grey: thin dashed arrows signify the partitioning of *de novo* (autotrophic) acetate H into the NADPH and H_2O pools, while the fraction (g) of acetate methyl groups that is inherited directly from organic substrates is shown with a long-dashed arrow; in *N. maritimus*, g is always zero. Details about the specific stoichiometry for each BP are shown in Figure 3 and Tables 2, 3, and S2.

Figure 3:

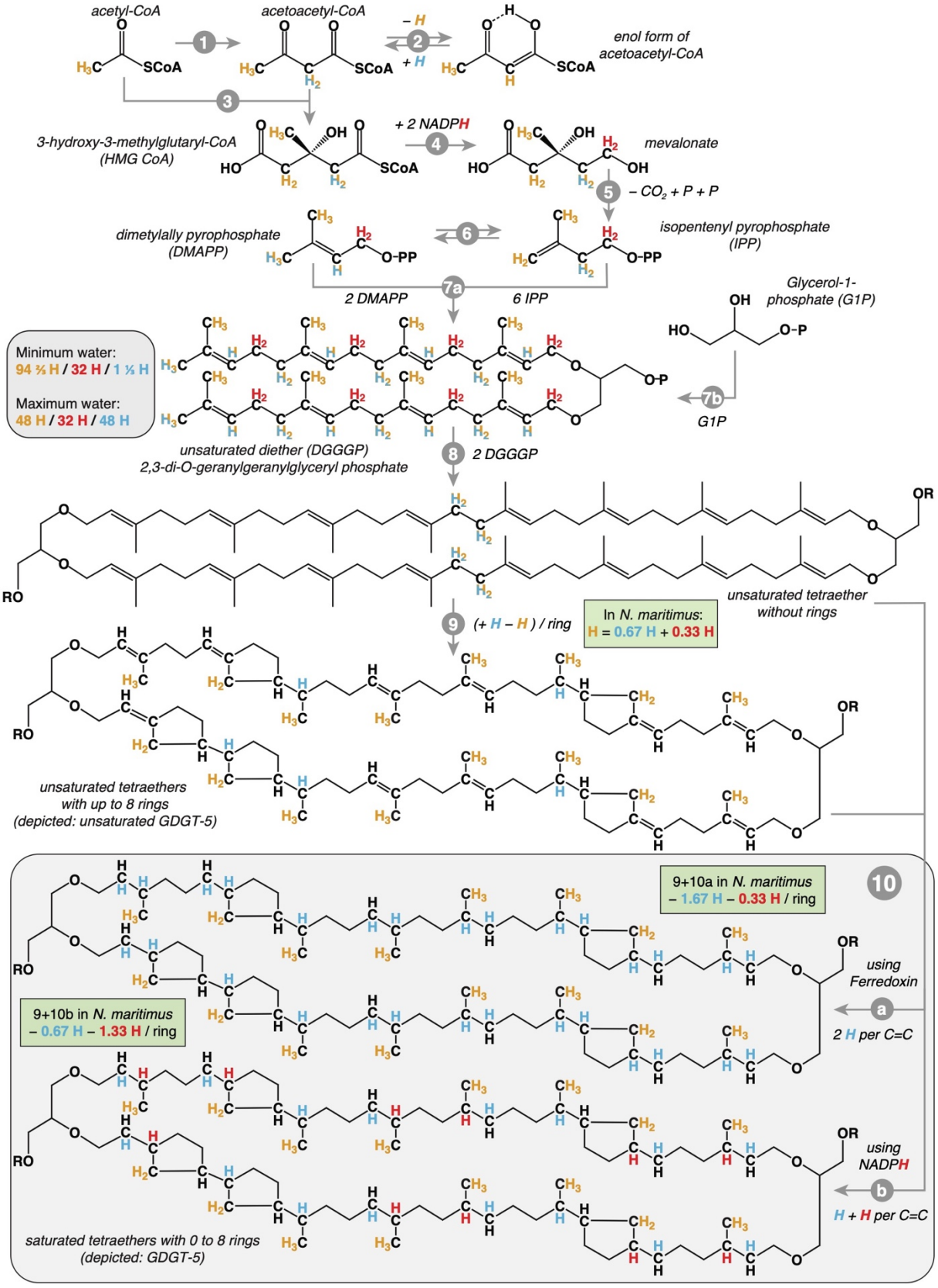
acetyl-CoA
acetoacetyl-CoA
– H
+ H
enol form of acetoacetyl-CoA
3-hydroxy-3-methylglutaryl-CoA (HMG CoA)
+ 2 NADPH
mevalonate
– CO2 + P + P
dimetylally pyrophosphate (DMAPP)
isopentenyl pyrophosphate (IPP)
2 DMAPP
6 IPP
Glycerol-1-phosphate (G1P)
G1P
Minimum water:
94 ⅔ H / 32 H / 1 ⅓ H
Maximum water:
48 H / 32 H / 48 H
unsaturated diether (DGGGP)
2,3-di-O-geranylgeranylglyceryl phosphate
2 DGGGP
unsaturated tetraether without rings
(+ H – H) / ring
In N. maritimus:
H = 0.67 H + 0.33 H
unsaturated tetraethers with up to 8 rings
(depicted: unsaturated GDGT-5)
9+10a in N. maritimus
– 1.67 H – 0.33 H / ring
using Ferredoxin
2 H per C=C
9+10b in N. maritimus
– 0.67 H – 1.33 H / ring
using NADPH
H + H per C=C
saturated tetraethers with 0 to 8 rings
(depicted: GDGT-5)

Figure 3. Overview of H sources for archaeal tetraether biosynthesis. Here (orange) H from acetyl-CoA; (red) H from NADPH; (blue) H from protons (water-derived H^+). Mixed potential sources of H from acetyl-CoA and water are shown half orange/half blue. For clarity, the H that enters lipid synthesis from acetyl-CoA methyl groups is visualized in orange; the biosynthetic sources of this H in *N. maritimus* are shown in Figure S4. The summary box for DGGGP indicates the minimum and maximum numbers of alkyl chain H that could originate from water during tetraether biosynthesis, which depends on the extent of re-equilibration during isomerization steps (2 & 6). See Tables 2, 3, and Table S2 for full accounting of the different scenarios. The net effect of ring formation on H sources combines the formation of the rings (step 9) with correspondingly fewer double bond reductions (step 10). The overall stoichiometry per ring for *N. maritimus* is a net of -1.67 H from water and -0.33 H from NADPH if the GGR pathway is reduction with Ferredoxin (steps 9 + 10a) or -0.67 H from water and -1.33 H from NADPH if NADPH is the cofactor (steps 9 + 10b). See the main text for further discussion. Biosynthetic steps are indicated in grey. 1: acetyl-CoA acetyl transferase; 2: tautomerization of acetoacetyl-CoA (can exchange the H at the C_2 position). 3: HMG CoA synthase; 4: HMG CoA reductase; 5: several alternative pathways from mevalonate to IPP (no H differences); 6: IPP isomerase (can exchange the H at the C_4 position); 7a: geranylgeranyl pyrophosphate synthase; 7b: geranylgeranyl glyceryl phosphate synthase; 8: tetraether synthase (Tes); 9: ring synthases (GrsAB); 10: geranylgeranyl reductase (GGR) using ferredoxin (a) or NADH/NADPH (b) as reductant.

Figure 4:

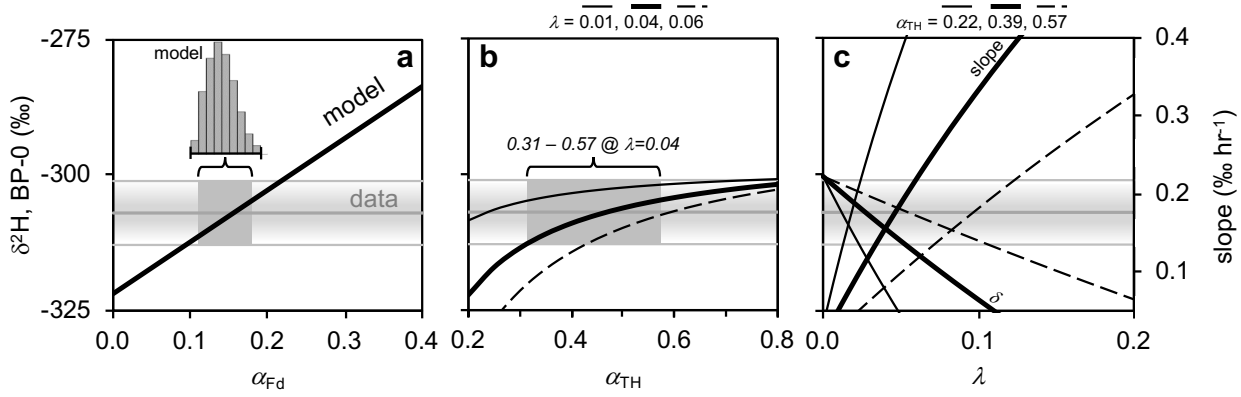

Figure 4. Sensitivity analysis. The Sensitivity of R_{BP} to model results; Scenario 2, $f_x = 0$, $f_{Fd} \neq 0$. Horizontal grey lines and shaded regions ("data") represent the mean and ± 1σ range for δ^2H values of BP-0 at average T_D. Black lines indicate model results, with dark grey boxes indicating where the model is compatible with the data. The inset histogram in (**a**) shows the frequency distribution of best-fit values of α_{Fd} (mean fit, 0.14 ± 0.02) for Scenario 2, Case A; this version yields $\alpha_E \bullet \alpha_{NADPH} = 0.669$ (Figure S6), *i.e.*, it does not prescribe a value for α_{NADPH}. Scenario 2, Case B yields exact values of $\alpha_{Fd} = 0.132$ and $\alpha_E = 0.743$ when α_{NADPH} is fixed at 0.9; see Table 4 and main text. (**b**) The strong co-dependence of α_{TH} and λ (Figure S6) indicates the minimum likely value of α_{TH} is > the 0.22 boundary value (from PntAB), and that the data would be compatible with values of $\alpha_{TH} > 0.57$ (from sTH) only if λ is > 0.6. (**c**) The predicted growth rate sensitivity (slope, ‰ hr^{-1}), and isotope ratio (negative-slope curves; δ^2H, ‰), are strongly dependent on λ. At the consensus $\alpha_{TH} = 0.39$ (thick lines), the permitted range of λ to satisfy values of δ^2H is ~0.01 – 0.06 (downward sloping thick black line). However, the growth rate sensitivity narrows this range to 0.03-0.05 (upward sloping thick black line). The consensus λ value using α_{TH} =0.39 and data for all compounds is $\lambda = 0.04$ (Table 4).

Figure 5:

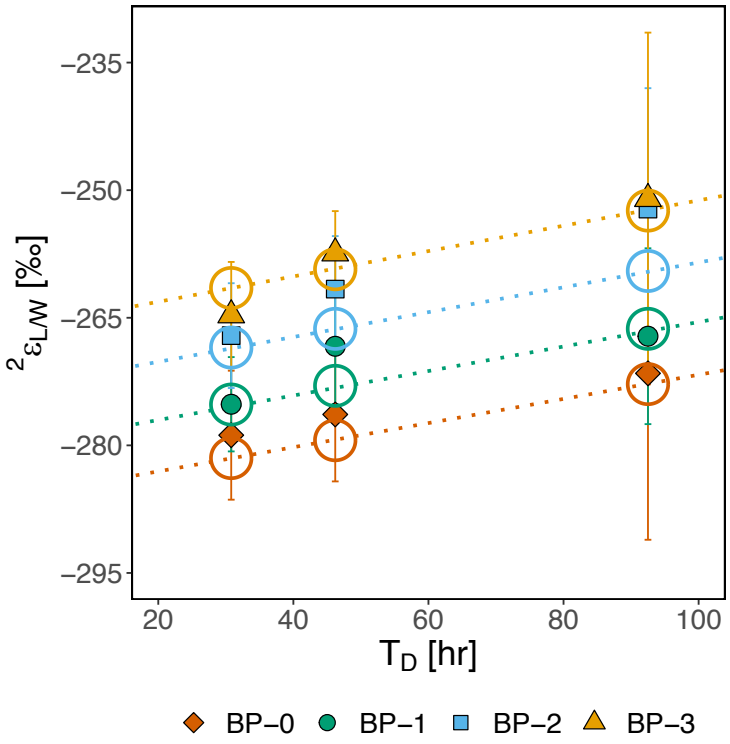

Figure 5. Model/data comparison. The $^2\varepsilon_{L/W}$ values for BPs of *N. maritimus* from models and measurements, showing growth-rate and ring-number dependence. Open symbols are the model simulation while closed symbols are the data; calculations use the consensus estimates of kinetic isotope effects for "Scenario 2", Table 4. The growth-rate effect, or slope of $^2\varepsilon_{L/W}$, is modeled to be 0.15 ‰ hr^{-1} (the data yield 0.2 ± 0.1 ‰ hr^{-1}; Figure 1). The ring-dependent enrichment of ^2H is modeled to be 6.7 ‰ $ring^{-1}$ (the data yield 6.4 ± 2.7 ‰ $ring^{-1}$).

Figure 6:

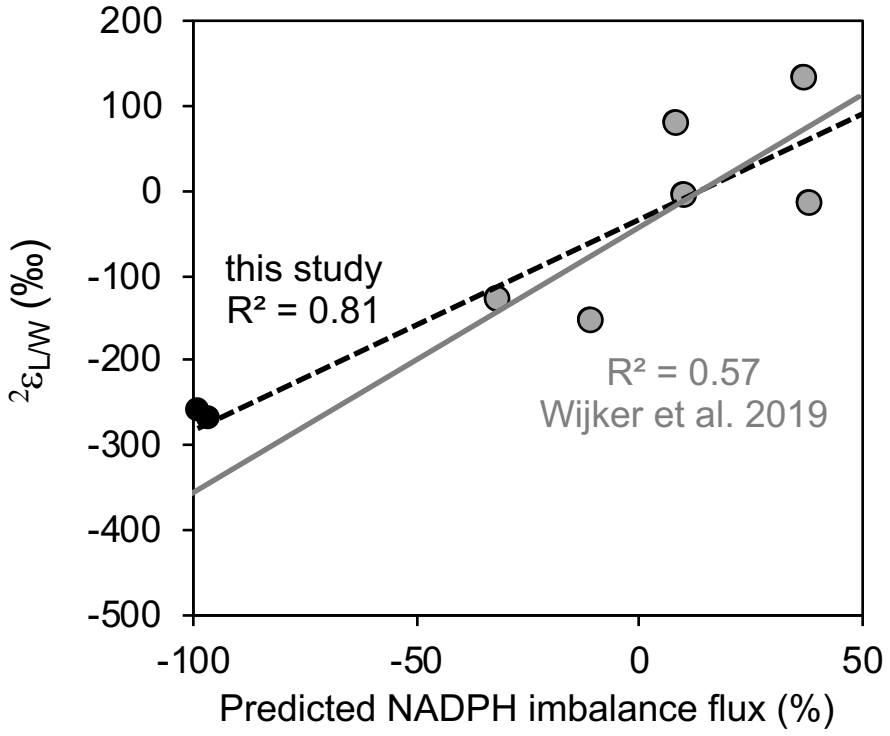

Figure 6. NADPH flux imbalance. Values for or *N. maritimus* agree with the linear dependence of bacterial $^2\varepsilon_{L/W}$ on relative NADPH availability (Wijker et al., 2019). In cells under extreme NADPH deficit, the minimum $^2\varepsilon_{L/W}$ value is predicted to be -282‰ (intercept of all data). This value not only indicates a consistent overall KIE for H cycling within cellular biosynthetic processes, it also agrees with the premise that archaea metabolize under conditions of extreme energy limitation (Valentine, 2007). Original Wijker et al. (2019) data and linear fit are shown in grey and solid line; our data and the new fit are in black and dashed line.

Main Tables 1 - 4

Table 1: Data for individual biphytanes per chemostat rate.

T_D (hr)	#	water δ^2H (‰)	BP-0 (‰) δ^2H	BP-0 (‰) $^2\varepsilon_{L/W}$	BP-1 (‰) δ^2H	BP-1 (‰) $^2\varepsilon_{L/W}$	BP-1 (‰) $\Delta\varepsilon$/ring	BP-2 (‰) δ^2H	BP-2 (‰) $^2\varepsilon_{L/W}$	BP-2 (‰) $\Delta\varepsilon$/ring	BP-3 (‰) δ^2H	BP-3 (‰) $^2\varepsilon_{L/W}$	BP-3 (‰) $\Delta\varepsilon$/ring	relative abundance (%) BP-0	BP-1	BP-2	BP-3	weighted avg. $^2\varepsilon_{L/W}$ (‰)
30.8	10	-44.0	-311 ± 7	-279 ± 8	-307 ± 5	-275 ± 6	3.6	-299 ± 6	-267 ± 6	7.0	-297 ± 6	-265 ± 6	4.1	27 ± 1	31 ± 1	25 ± 1	17 ± 1	-272 ± 6
46.2	6	-42.0	-307 ± 8	-276 ± 8	-299 ± 6	-268 ± 7	8.0	-293 ± 6	-262 ± 6	7.0	-289 ± 5	-257 ± 5	5.3	22 ± 1	24 ± 1	32 ± 1	22 ± 1	-266 ± 7
92.5	4	-44.0	-304 ± 19	-272 ± 20	-299 ± 10	-267 ± 10	4.4	-285 ± 14	-252 ± 14	12.3	-284 ± 19	-251 ± 20	5.4	17 ± 1	32 ± 1	29 ± 1	21 ± 1	-260 ± 8

	$^2\varepsilon_{L/W}$	$\Delta^2\varepsilon$/ring
Average (all BPs)	-266 ± 9 ‰	6.4 ± 2.7 ‰

* Data and processing scripts for GC-P-IRMS output are available at: https://github.com/KopfLab/2022_leavitt_et_al.

Table 2: Stoichiometric summary of hydrogen sources to archaeal BP-0. Detailed stoichiometry in Table S1.

Biosynthetic Scenarios	BP-0 ($C_{40}H_{80}$)				
	Ac-CoA	H_2O	NAD(P)H	Fd (H^-)	H_2O-Exch
	f_A	f_{GGR_W} $f_{LipSynth\_W}$	f_{GGR_NADPH} $f_{LipSynth\_NADPH}$	f_{GGR_Fd}	f_x
Scenario 1:	47 ⅓	8 ⅔	8 16	0	0
Scenario 2:	47 ⅓	8 ⅔	0 16	8	0
Scenario 3:	24	8 0	8 16	0	24
Scenario 4:	24	8 0	0 16	8	24

Table 3: Changes in biosynthetic H source for ring-containing biphytanes relative to BP-0 for organisms producing Ac-CoA autotrophically via the 3HP/4HB pathway. Details in Table S1.

		$(f_{*W} + f_x)$	f_{*NADPH}	f_{Fd}
Scenario 1	BP-1	0.43%	-0.43%	--
	BP-2	0.89%	-0.89%	--
	BP-3	1.37%	-1.37%	--
Scenario 2	BP-1	0.43%	0.59%	-1.03%
	BP-2	0.89%	1.21%	-2.11%
	BP-3	1.37%	1.87%	-3.24%
Scenario 3	BP-1	0.68%	-0.68%	--
	BP-2	1.40%	-1.40%	--
	BP-3	2.16%	-2.16%	--
Scenario 4	BP-1	0.68%	0.34%	-1.03%
	BP-2	1.40%	0.70%	-2.11%
	BP-3	2.16%	1.08%	-3.24%

Table 4: Model results for KIEs α_W, α_{TH}, α_E, α_{Fd}, and α_{NADPH}, and flux coefficient λ.

Parameter	Scenario 2, Case A	Scenario 2, Case B
α_W	≥ 0.9	set, 0.9
α_{Fd}	0.14 ± 0.02	0.132
α_{NADPH}	product = 0.669	set, 0.9
α_E		0.743
α_{TH}	range, 0.22-0.57[a]	
λ	range, 0.013-0.061	

[a] Minimum and maximum KIE of hypothetical transhydrogenation, set as the limits of soluble and membrane-bound transhydrogenase KIEs reported in Wijker et al., 2019.

Supplemental Figures 1 - 6

Figure S1: All Biphytane H-Isotope Data

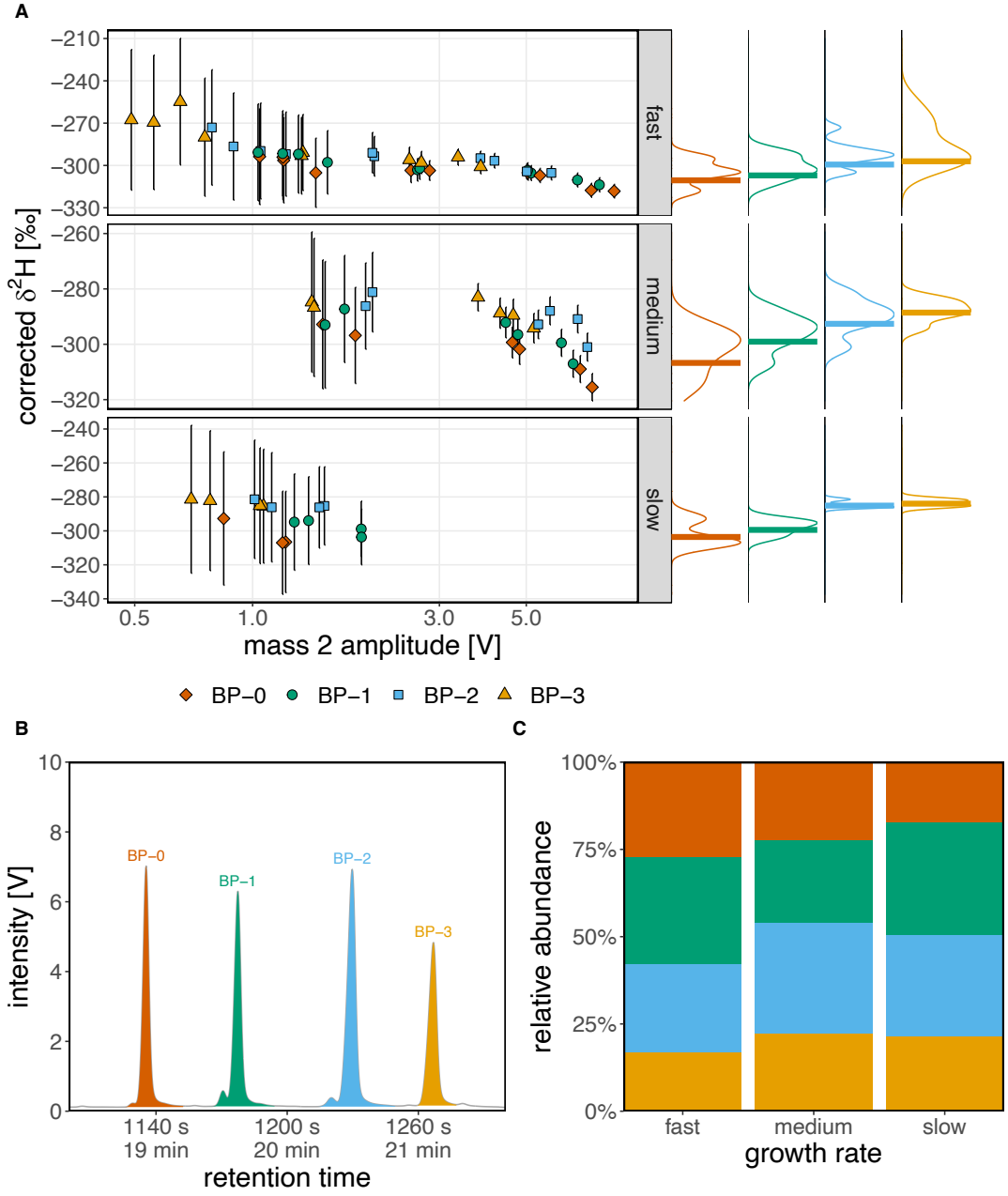

Figure S1. (A) Replicate hydrogen isotope measurements of archaeal biphytanes (BPs) from *N. maritimus*. All isotope values are calibrated against the A6 alkane standard and corrected for alkyl iodide hydrogenation (δ^2H_{cor}) with propagated errors (σ_{cor}) from hydrogenation and peak-size adjusted uncertainties as described in the methods section. (**B**) Example chromatogram showing mass-2 trace of GC-P-IRMS analysis with BPs highlighted. (**C**) Relative abundances of BPs at the "Fast", "Medium", and "Slow" growth rates used in this study (see Table 1 for doubling times).

Figure S2: IRMS Calibration

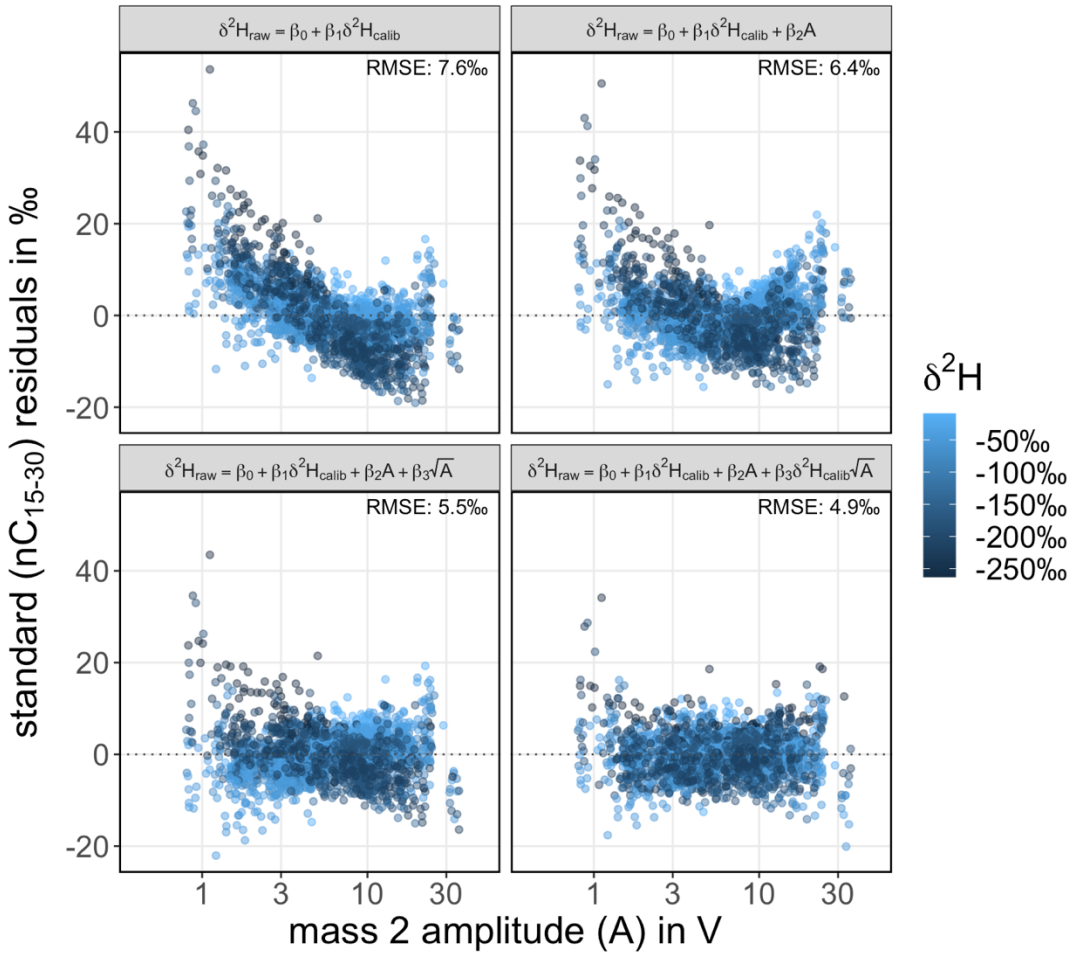

Figure S2. Residuals of the 2195 compound-specific H isotope measurements from the A6 standard compounds (C_{15} through C_{30} *n*-alkanes) using 4 different multivariate linear calibration models. The regression equation and root-mean-square error (RMSE) of each model are shown in their respective panel. The regression model whose residuals are shown in the lower right panel ($\delta^2H_{raw} = \beta_0 + \beta_1 \cdot \delta^2H_{cal} + \beta_2 \cdot A + \beta_3 \cdot \delta^2H_{cal} \cdot \sqrt{A}$, RMSE 4.9 ‰) is the one used for calibration as discussed in the main text.

Figure S3: H-Isotope Absolute Error Estimates

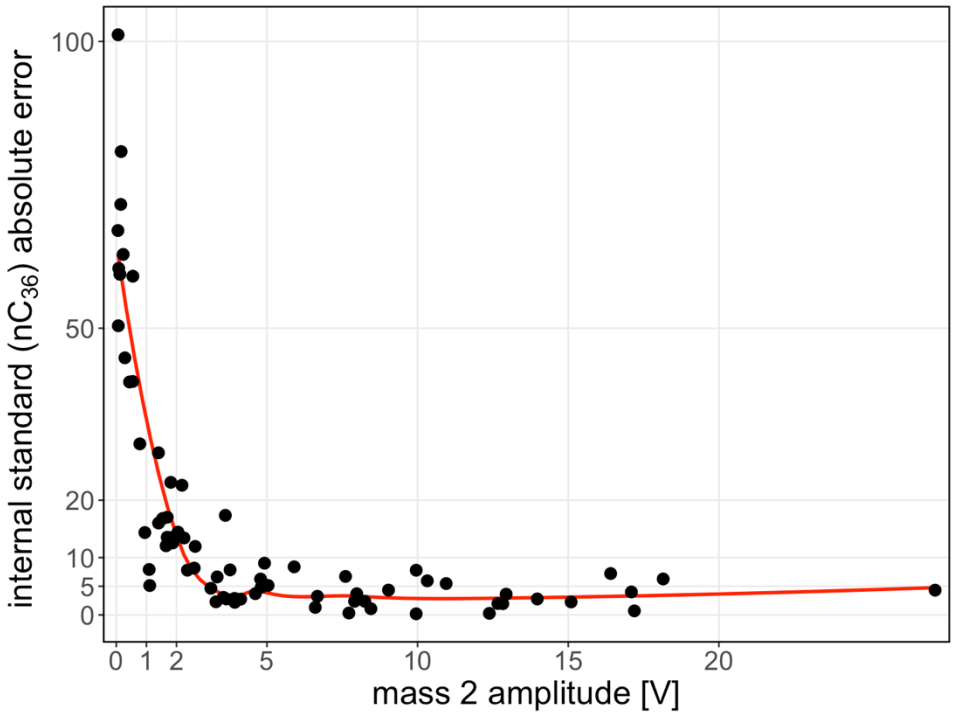

Figure S3. Absolute error of the calibrated δ^2H_{cal} values of the nC_{36} standard (n=73) vs its known isotopic composition. The red line represents a local polynomial regression fit and was used to determine peak-sized adjusted error estimates for the δ^2H_{cal} values (σ_{cal}) of the measured biphytanes (Figures 1 and S1).

Figure S4: 3HP/4HP

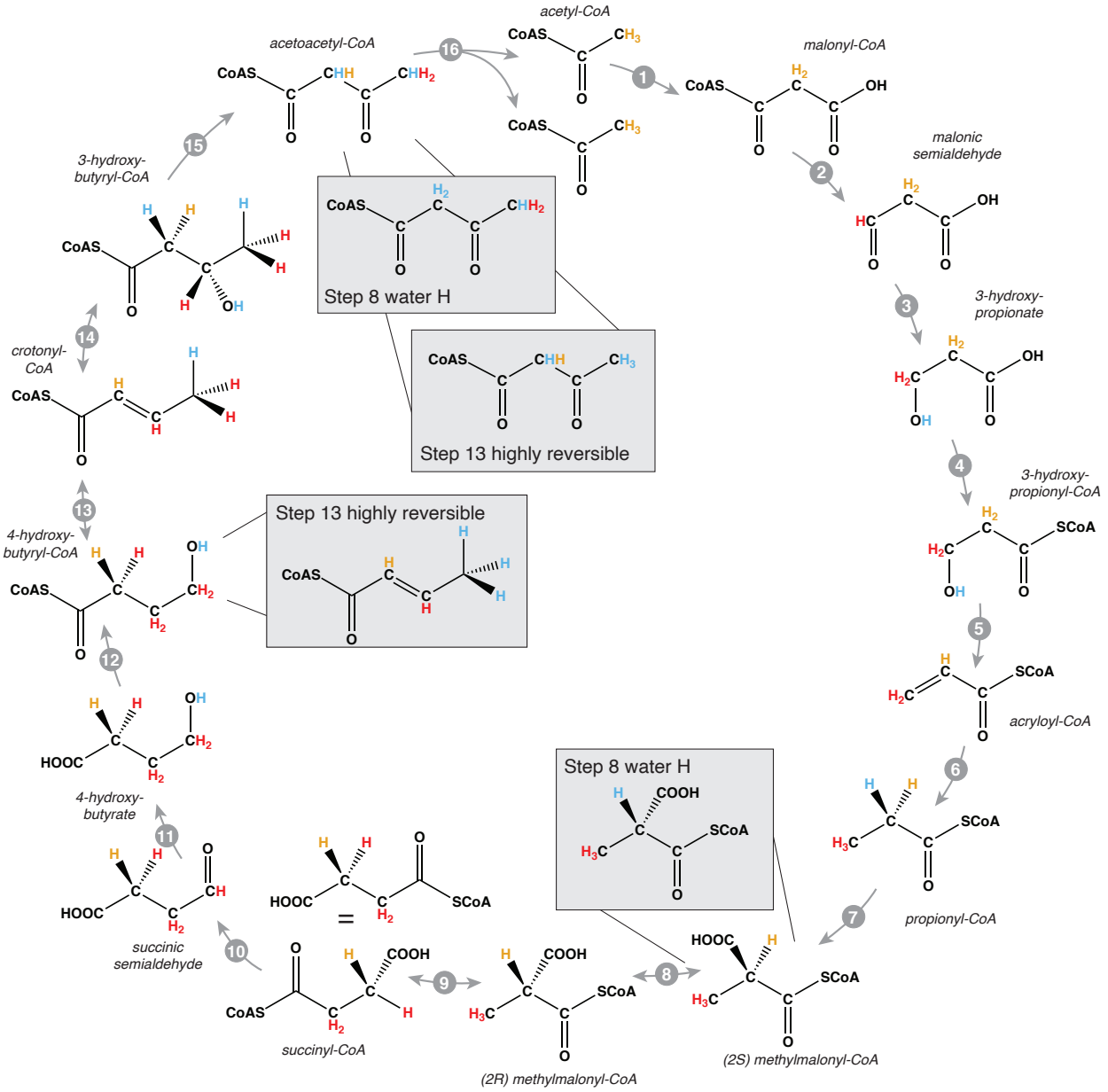

Figure S4. Origin of the methyl group hydrogens of acetyl-CoA derived from the 3HP/4HP (3-hydroxyproprionate / 4-hydroxybutyrate) cycle. The H from water (protons) are shown in blue; H from NADPH in red. One full turn of the cycle generates newly biosynthesized acetyl-CoA (orange) in which all H were originally derived from water and NADPH; all, or all but one, of these H are replaced by the next turn of the cycle. The color coding shows H sources for the maximum efficiency and stereospecificity of all enzymes: the resulting acetoacetyl-CoA incorporates 60% H from water and 40% H from NADPH (maximum possible from NADPH). Methylmalonyl-CoA epimerase (step 8) has a high likelihood of introducing water H at the α-C ("Step 8 water H") (WÖLFLE *et al.*, 1986), thus removing the H from the original acetyl CoA: the resulting acetyl-CoA incorporates 2/3 (66.67%) H from water and 1/3 (33.33%) H from

NADPH. If 4-hydroybutyryl-CoA dehydratase (step 13) is highly reversible under physiological conditions, the 2 H at the ω-C also can be fully exchanged with H from water (Friedrich *et al.*, 2008): the resulting acetyl-CoA ("Step 13 highly reversible") would then incorporate 100% water-H and 0% from NADPH. We consider water introduction at step 8 highly likely, but preserve the original H at step 13, and thus base the modelling discussed in the main text on this scenario. Enzymatic steps are indicated with grey arrows. 1: Acetyl-CoA carboxylase, 2: Malonyl CoA reductase, 3: Malonic semialdehyde reductase, 4: 3-hydroxypropionyl-CoA synthetase, 5: 3-hydroxypropionyl-CoA dehydratase, 6: Acryloyl-CoA reductase, 7: Propionyl-CoA carboxylase, 8: Methylmalonyl CoA epimerase, 9: Methylmalonyl-CoA mutase, 10: Succinyl-CoA reductase, 11: Succinic semialdehyde reductase, 12: 4-Hydroxybutyryl-CoA synthetase, 13: 4-Hydroxybutyryl-CoA dehydratase, 14: Crotonyl-CoA hydratase, 15: 3-Hydroxybutyryl-CoA dehydrogenase, 16: Acetoacetyl-CoA β-ketothiolase. Most carboxylic acids are partly deprotonated at physiological pH but are shown fully protonated for simplicity.

Figure S5: Stoichiometric Fluxes

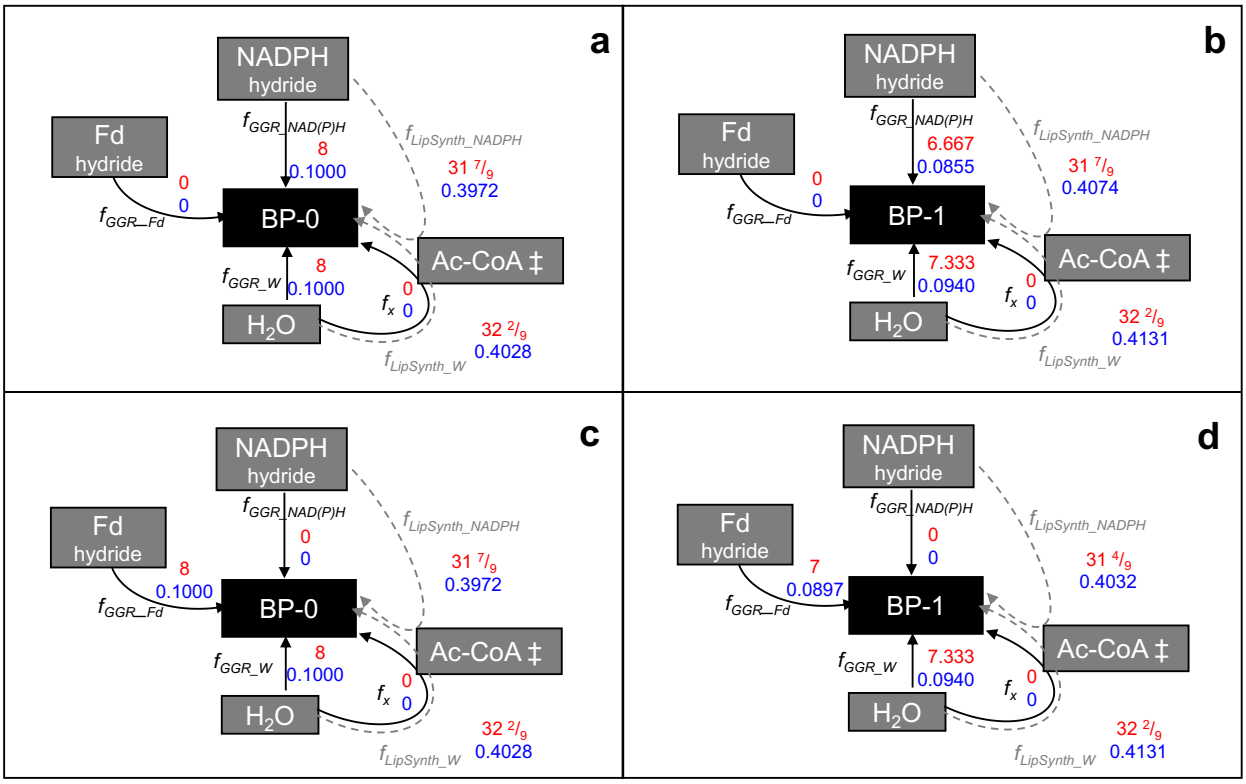

Figure S5. Details of the stoichiometric fluxes of anabolic hydrogen for archaeal lipid biosynthesis (see Figure 2 for schematic overview), showing absolute (red) and relative (blue) stoichiometry for BP-0 (**a**, **c**) and BP-1 (**b**, **d**); other BPs beyond BP-1 change proportionally (Table 3, Table S2). The two potential hydride sources for geranylgeranyl reductase (GGR) are NAD(P)H (**a**, **b**) and ferredoxin (Fd; **c**, **d**), with the paired proton derived in each case from water (f_{GGR_W}). The other protons that form the BP polyprene chains are inherited from Ac-CoA and gained from NADPH during synthesis of IPP; one additional proton from water enters via DMAPP/IPP isomerization (Figure 2, step 6), resulting in the usual fractional distribution between $f_{LipSynth\_W}$ and $f_{LipSynth\_NADPH}$. Ac-CoA also is permitted in some modeled scenarios to exchange protons with water during keto/enol tautomerization (Figure 2, step 2; f_x) although in the four examples shown here this value is set to zero.

Figure S6: Model Dependencies

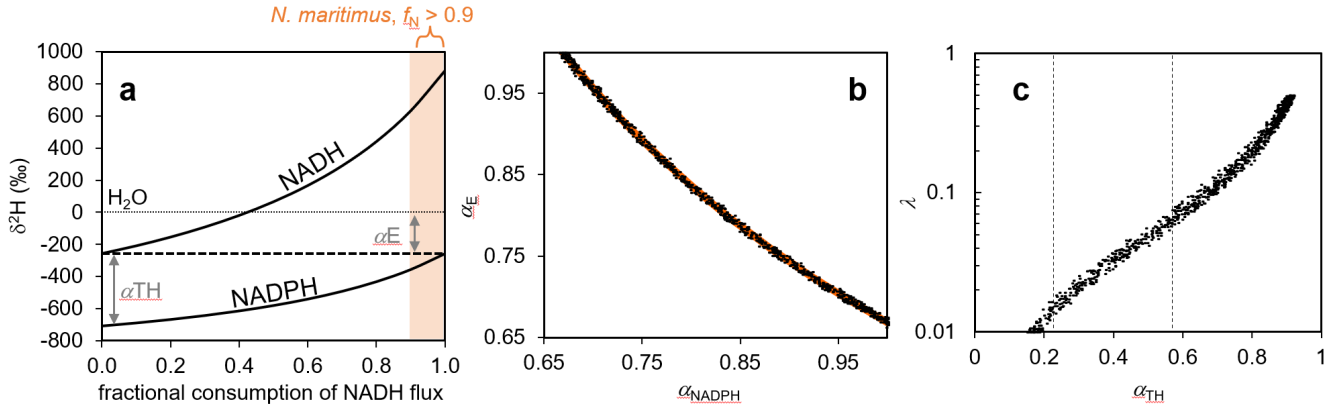

Figure S6. (**a**) Co-dependence of δ^2H of the NADH and NADPH pools generated by Cellular production (Figure 4, Eq. 11). Co-dependence of (**b**) α_E and α_{NADPH} and (**c**) λ and α_{TH}, across all variable space of the initial conditions of Scenario 2, calculated for R_{BP} from the isotope flux balance of biphytane synthesis (Figure 4; Eq. 13). Individual data points are Monte Carlo simulation results. Orange curve in (**b**): $y = 0.669/x$. Boundaries (dashed lines) in (**c**) mark the suggested minimum and maximum values of α_{TH} (0.222, PntAB; 0.566 sTH; Wijker et al., 2019). The observed range suggests λ is no greater than ~0.06 (6% inefficiency of NADH hydride transfer; main text Figure 4).

Supplemental References:

Friedrich, P., Darley, D.J., Golding, B.T., and Buckel, W. (2008) The Complete Stereochemistry of the Enzymatic Dehydration of 4-Hydroxybutyryl Coenzyme A to Crotonyl Coenzyme A. *Angew Chem Int Ed* **47**: 3254–3257.

Leavitt, W.D., Flynn, T.M., Suess, M.K., and Bradley, A.S. (2016) Transhydrogenase and Growth Substrate Influence Lipid Hydrogen Isotope Ratios in Desulfovibrio alaskensis G20. *Front Microbiol* **07**:

WÖLFLE, K., MICHENFELDER, M., KÖNIG, A., HULL, W.E., and RÉTEY, J. (1986) On the mechanism of action of methylmalonyl-CoA mutase: Change of the steric course on isotope substitution. *Eur J Biochem* **156**: 545–554.

Supplemental Tables 1 & 2

Supplemental Table S1: Hydrogen Sources.

Full accounting of H sources to the biphytanes of archaeal tetraethers for organisms producing acetyl-CoA autotrophically via the 3HP/4HB pathway (assuming water H:NADPH = 2:1, i.e., 0.6667:0.3333. See also main text Figure 3, and main text Tables 2, 3. Raw data and processing scripts for GC-P-IRMS output are available at: https://github.com/KopfLab/2022_leavitt_et_al.

			Number of H in Biphytane				Fractions - detailed				Fractions-simplified			
							f_{GGR_W} / $f_{LipSynth\_W}$	$f_{GGR\_NAD(P)H}$ / $f_{LipSynth\_NADPH}$	f_{GGR_Fd} / n/a	n/a / f_x	f_{*W}	f_{*NADPH}	f_{Fd}	f_x
			H_2O	NADPH	Fd	H_2O_Exch	H_2O	NADPH	Fd	H_2O_Exch	H_2O	NADPH	Fd	H_2O_Exch
Scenario 1	**BP0**	GGR	8	8	0	--	0.1000	0.1000	0	--	0.5028	0.4972	0	0
		LipSynth	32.222	31.778	--	0	0.4028	0.3972	--	0				
	BP1	GGR	7.333	7	0	--	0.0940	0.0897	0	--	0.5071	0.4929	0	0
		LipSynth	32.222	31.444	--	0	0.4131	0.4031	--	0				
	BP2	GGR	6.667	6	0	--	0.0877	0.0789	0	--	0.5117	0.4883	0	0
		LipSynth	32.222	31.111	--	0	0.4240	0.4094	--	0				
	BP3	GGR	6.000	5	0	--	0.0811	0.0676	0	--	0.5165	0.4835	0	0
		LipSynth	32.222	30.778	--	0	0.4354	0.4159	--	0				
Scenario 2	**BP0**	GGR	8	0	8	--	0.1000	0	0.1000	--	0.5028	0.3972	0.1000	0
		LipSynth	32.222	31.778	--	0	0.4028	0.3972	--	0				
	BP1	GGR	7.333	0	7	--	0.0940	0	0.0897	--	0.5071	0.4031	0.0897	0
		LipSynth	32.222	31.444	--	0	0.4131	0.4031	--	0				
	BP2	GGR	6.667	0	6	--	0.0877	0	0.0789	--	0.5117	0.4094	0.0789	0
		LipSynth	32.222	31.111	--	0	0.4240	0.4094	--	0				
	BP3	GGR	6.000	0	5	--	0.0811	0	0.0676	--	0.5165	0.4159	0.0676	0
		LipSynth	32.222	30.778	--	0	0.4354	0.4159	--	0				
Scenario 3	**BP0**	GGR	8	8	0		0.1000	0.1000	0		0.3000	0.4000	0	0.3000
		LipSynth	16	24	--	24	0.2000	0.3000	--	0.3000				
	BP1	GGR	7.333	7	0		0.0940	0.0897	0		0.2991	0.3932	0	0.3077
		LipSynth	16	23.667	--	24	0.2051	0.3034	--	0.3077				
	BP2	GGR	6.667	6	0		0.0877	0.0789	0		0.2982	0.3860	0	0.3158
		LipSynth	16	23.333	--	24	0.2105	0.3070	--	0.3158				
	BP3	GGR	6.000	5	0		0.0811	0.0676	0		0.2973	0.3784	0	0.3243
		LipSynth	16	23.000	--	24	0.2162	0.3108	--	0.3243				
Scenario 4	**BP0**	GGR	8	0	8		0.1000	0	0.1000		0.3000	0.3000	0.1000	0.3000
		LipSynth	16	24	--	24	0.2000	0.3000	--	0.3000				
	BP1	GGR	7.333	0	7		0.0940	0	0.0897		0.2991	0.3034	0.0897	0.3077
		LipSynth	16	23.667	--	24	0.2051	0.3034	--	0.3077				
	BP2	GGR	6.667	0	6		0.0877	0	0.0789		0.2982	0.3070	0.0789	0.3158
		LipSynth	16	23.333	--	24	0.2105	0.3070	--	0.3158				
	BP3	GGR	6.000	0	5		0.0811	0	0.0676		0.2973	0.3108	0.0676	0.3243
		LipSynth	16	23.000	--	24	0.2162	0.3108	--	0.3243				

Supplemental Table S2: NADP(H) Source Mechanisms in *N. maritimus.* BLAST approach employed as by (Leavitt et al., 2016).

Enzyme name	***NAD(P)H generating***	***Abbreviation***	***H-isotope category***	***Pathway***	***Nitrosopumilus maritimus SCM1 locus tag(s)***
Complex 1: NADH:ubiquinone oxidoreductase	Yes	Nuo	2b	N/A	N_mar_0276 to 0286
Ferredoxins	Yes	Fd	2b, 3	N/A	N_mar_0238, 0239, 1537, 1765
ferredoxin:NADP+ oxidoreductase	Yes	FNR	*3*	N/A	Nmar_0672
cytosolic NADP+-reducing hydrogenase	Yes	SH	3 or 2	N/A	Nmar_1389
cytosolic NADP+-reducing hydrogenase	Yes	SH	3 or 2	N/A	Nmar_0267
cytosolic NADP+-reducing hydrogenase	Yes	SH	3 or 2	N/A	Nmar_0253
NAD+ kinase	Yes	NADK	2	N/A	Nmar_0268, Nmar_0440, Nmar_0921
isocitrate dehydrogenase	Yes	IDH	2	TCA cycle	Nmar_1069, Nmar_1379
glucose-6-phosphate dehydrogenase	Yes	G6PDH	2	oxPPP, ED	Nmar_0168
6-phosphogluconate dehydrogenase	Yes	6PGDH	2	oxPPP	Nmar_0635
glucose dehydrogenase	Yes	GDHs	2	Modified EDs	Nmar_0369
non-phosphorylating glyceraldehyde 3-phosphate dehydrogenase	Yes	GAPN	2	EMP, ED, SP ED	Nmar_1608
NAD+-dependent glyceraldehyde phosphate dehydrogenase, phosphorylating	Yes	NAD+/GAPDH	2	EMP, ED, SP ED	Nmar_0831
D-glyceraldehyde dehydrogenase (NADP+)	Yes	NADP+/GADH	2	npED	Nmar_1608
2-ketoglutarate (oxoacid)/ ferredoxin oxidoreductase			2	TCA cycle	Nmar_0413, Nmar_0414
malate dehydrogenase	Yes		2	TCA cycle	Nmar_0338, Nmar_0676

/END